

Deciphering the Physical Origin of GRB 240825A: A Long GRB Lacking a Bright Supernova

RAHUL GUPTA,^{1,2} JUDITH RACUSIN,¹ R. SÁNCHEZ-RAMÍREZ,³ Y.-D. HU,^{4,5} A. ROSSI,⁶ M. D. CABALLERO-GARCÍA,³ PI NUESSLE,^{7,1} A. J. CASTRO-TIRADO,^{3,8} S. R. OATES,⁹ P. P. BORDOLOI,¹⁰ A. ARYAN,¹¹ S. DICHARA,¹² P. VERES,^{13,14} N. KLINGLER,¹ N. OMODEI,¹⁵ E. MAIORANO,⁶ D. TAK,¹⁶ S. SHILLING,⁹ J. E. ADSUARA,¹⁷ P. H. CONNELL,¹⁷ E. FERNÁNDEZ-GARCÍA,³ G. GARCÍA-SEGURA,^{18,3} A. GHOSH,¹⁹ E. GÖĞÜŞ,²⁰ F. J. GORDILLO-VÁZQUEZ,³ M. GRITSEVICH,^{21,22,23} A. N. GUELBEZU,²⁴ S. GUZİY,^{3,25,26} L. HANLON,²⁷ H. J. VAN HEERDEN,²⁸ S. IYANI,^{10,29} A. MARTIN-CARRILLO,²⁷ P. J. MEINTJES,²⁸ J. NAVARRO-GONZÁLEZ,¹⁷ T. NEUBERT,³⁰ N. ØSTGAARD,³¹ S. B. PANDEY,³² I. PÉREZ-GARCÍA,³ S. RAZZAQUE,^{19,7,33} E. SONBAS,^{34,7} SI-YU WU,³ A. POZANENKO,³⁵ A. VOLNOVA,³⁶ A. MOSKVITIN,³⁷ S. BELKIN,³⁸ O. SPIRIDONOVA,³⁷ O. BURKHONOV,³⁹ SH. EGAMBERDIYEV,^{39,40} E. KLUNKO,⁴¹ V. RUMYANTSEV,⁴² I. SOKOLOV,⁴³ A. NOVICHONOK,⁴⁴ I. REVA,⁴⁵ A. VOLVACH,⁴² AND L. VOLVACH⁴²

¹*Astrophysics Science Division, NASA Goddard Space Flight Center, Mail Code 661, Greenbelt, MD 20771, USA*

²*NASA Postdoctoral Program Fellow*

³*Instituto de Astrofísica de Andalucía (IAA-CSIC), Glorieta de la Astronomía s/n, E-18008, Granada, Spain*

⁴*Guangxi Key Laboratory for Relativistic Astrophysics, School of Physical Science and Technology, Guangxi University, Nanning 530004, China*

⁵*INAF-Osservatorio Astronomico di Brera, Via E. Bianchi 46, 23807 Merate, LC, Italy*

⁶*INAF – Osservatorio di Astrofisica e Scienza dello Spazio, Via Piero Gobetti 93/3, 40129 Bologna, Italy*

⁷*Department of Physics, The George Washington University, 725 21st St. NW, Washington, DC 20052, USA*

⁸*Ingeniería de Sistemas y Automática, Universidad de Málaga, Unidad Asociada al CSIC por el IAA, Escuela de Ingenierías Industriales, Arquitecto Francisco Peñalosa, 6, Campanillas, 29071 Málaga, Spain*

⁹*Department of Physics, Lancaster University, Lancaster, LA1 4YB, UK*

¹⁰*Indian Institute of Science Education and Research, Thiruvananthapuram, Kerala, India, 695551*

¹¹*Graduate Institute of Astronomy, National Central University, 300 Jhongda Road, 32001 Jhongli, Taiwan*

¹²*Penn State Univ, Dept Astron & Astrophys, 525 Davey Lab, University Pk, PA 16802 USA*

¹³*Department of Space Science, University of Alabama in Huntsville, Huntsville, AL 35899, USA*

¹⁴*Center for Space Plasma and Aeronomic Research, University of Alabama in Huntsville, Huntsville, AL 35805, USA*

¹⁵*SLAC National Accelerator Laboratory, Stanford University, Stanford, CA 94305, USA*

¹⁶*SNU Astronomy Research Center, Seoul National University, Seoul 08826, Republic of Korea*

¹⁷*Image Processing Laboratory, University of Valencia, Paterna, Valencia, Spain*

¹⁸*Instituto de Astronomía, Universidad Nacional Autónoma de México, Carr. Tijuana-Ensenada km.107, 22860 Ensenada, B.C., Mexico*

¹⁹*Centre for Astro-Particle Physics (CAPP) and Department of Physics, University of Johannesburg, PO Box 524, Auckland Park 2006, South Africa*

²⁰*Sabancı University, Faculty of Engineering and Natural Sciences, İstanbul 34956 Türkiye*

²¹*Swedish Institute of Space Physics (IRF), Bengt Hultqvists väg 1, 981 92 Kiruna, Sweden*

²²*University of Helsinki, Faculty of Science, Gustav Hållströmin katu 2, FI-00014, Finland*

²³*Institute of Physics and Technology, Ural Federal University, Mira str. 19, 620002 Ekaterinburg*

²⁴*Thüringer Landessternwarte Tautenburg, Sternwarte 5, 07778 Tautenburg, Germany*

²⁵*Petro Mohyla Black Sea National University, Mykolaiv 54000, Ukraine*

²⁶*Mykolaiv Astronomical Observatory, Mykolaiv 54030, Ukraine*

²⁷*School of Physics and Centre for Space Research, University College Dublin, Belfield, Dublin 4, Ireland*

²⁸*Department of Physics, University of the Free State, 205 Nelson Mandela Drive, Bloemfontein, 9300, South Africa*

²⁹*High Performance Computing Centre, IISER Thiruvananthapuram, Kerala, India, 695551*

³⁰*National Space Institute, Technical University of Denmark, Kgs. Lyngby, Denmark*

³¹*Birkeland Centre for Space Science, Department of Physics and Technology, University of Bergen, Norway*

³²*Aryabhatta Research Institute of Observational Sciences (ARIES), Manora Peak, Nainital-263002, India*

³³*National Institute for Theoretical and Computational Sciences (NITheCS), Private Bag X1, Matieland, South Africa*

³⁴*Department of Physics, Adiyaman University, 02040 Adiyaman, Türkiye*

³⁵*Faculty of Physics, Higher School of Economics, Moscow 101000, Russia*

³⁶*Sternberg Astronomical Institute, Moscow State University, Russia*

³⁷*Special Astrophysical Observatory, Russian Academy of Sciences, Nizhny Arkhyz 369167, Russia*

Corresponding author: Rahul Gupta

rahul.gupta@nasa.gov, rahulbhu.c157@gmail.com

³⁸*School of Physics & Astronomy, Monash University, Clayton VIC 3800, Australia*

³⁹*Ulugh Beg Astronomical Institute, Uzbek Academy of Sciences, Tashkent 100052, Uzbekistan*

⁴⁰*National University of Uzbekistan, Tashkent, Uzbekistan*

⁴¹*Institute of Solar-Terrestrial Physics, Russian Academy of Sciences (Siberian Branch), Irkutsk 664033, Russia*

⁴²*Crimean Astrophysical Observatory, Russian Academy of Sciences, Nauchnyy 298409, Crimea*

⁴³*Institute of Astronomy of the Russian Academy of Science, Moscow, Russia*

⁴⁴*Petrozavodsk State University, 185910, Petrozavodsk, Karelia, Russia*

⁴⁵*Fesenkov Astrophysical Institute, Observatory street 23, Almaty 050020, Kazakhstan*

ABSTRACT

We present a comprehensive multiwavelength analysis of GRB 240825A, a bright gamma-ray burst (GRB) detected by *Fermi* and *Swift*, with a prompt duration ($T_{90} \sim 4$ sec in 50–300 keV) near the boundary separating short and long GRBs, prompting a detailed investigation into its classification and progenitor. Using classical prompt metrics (duration, minimum variability timescale (MVT), lag, and spectral hardness) and modern classification techniques (machine-learning (ML) based t-SNE, support vector machine, energy-hardness-duration, and $\varepsilon \equiv E_{\gamma, \text{iso}, 52} / E_{p, z, 2}^{5/3}$), we find GRB 240825A exhibits hybrid characteristics. The short MVT (13.830 ± 1.574 ms), rest-frame duration, and ML-based classification indicate a merger-like or ambiguous nature, while its energetics and position on the Amati relation favor a collapsar origin. We conducted deep optical and NIR photometric and spectroscopic late-time search for an associated supernova (SN)/kilonova (KN) and the host galaxy using 10.4m GTC and 8.4m binocular LBT telescopes. No bright SN (like SN 1998bw) is detected down to stringent limits (e.g., $m_r > 26.1$ mag at 17.59 days), despite a redshift of $z = 0.659$ measured from GTC spectroscopy. Host galaxy SED modeling with *Prospector* indicates a massive, dusty, and star-forming galaxy—typical of collapsar GRB hosts, though with low sSFR and large offset. We compare these findings with hybrid events like GRB 211211A, GRB 230307A, GRB 200826A, including SNe-GRBs, and conclude that GRB 240825A likely originated from a massive star collapse, possibly with an obscured or faint SN in a dusty host. This study emphasizes the need for multiwavelength follow-up and a multi-layered classification to determine GRB progenitors.

Keywords: Gamma-ray bursts (629) — High Energy astrophysics (739)

1. INTRODUCTION

Gamma-ray bursts (GRBs) are the most energetic electromagnetic phenomena known in the universe, releasing up to 10^{55} erg (E. Burns et al. 2023) of energy within seconds (T. Piran 2004). Since their serendipitous discovery by the Vela satellites in the late 1960s (R. W. Klebesadel et al. 1973), the understanding of these enigmatic events has evolved considerably, reflecting advancements in observational capabilities and theoretical modeling (G. J. Fishman & C. A. Meegan 1995; P. Kumar & B. Zhang 2015). They are broadly divided into two main classes—short and long—based on their observed durations (T_{90} , the time interval containing 90% of the burst’s fluence, C. Kouveliotou et al. 1993), and spectral hardness (the ratio of counts in the hard energy band to those in the soft energy band, A. Lien et al. 2016). This dichotomy, first revealed by the Burst and Transient Source Experiment (BATSE) onboard the *Compton Gamma Ray Observatory*, has served as a foundation for understanding GRB progen-

itors. Long-duration GRBs (LGRBs, $T_{90} > 2$ sec) typically have softer photon spectra than short-duration GRBs (SGRBs, $T_{90} \leq 2$ sec).

The physical association of LGRBs with the core-collapse of massive, rapidly rotating stars (S. E. Woosley 1993; A. I. MacFadyen & S. E. Woosley 1999), sometimes accompanied by broad-lined Type Ibc SNe (J. Hjorth et al. 2003; S. E. Woosley & J. S. Bloom 2006), and SGRBs with compact binary mergers such as binary neutron star or neutron star–black hole systems (E. Nakar 2007; E. Berger 2014a), provided an initial physical basis for the T_{90} -based dichotomy. The association of SGRBs with mergers was strengthened by the landmark multi-messenger observation of GRB 170817A and the gravitational wave event GW170817 (B. P. Abbott et al. 2017a,b; A. Goldstein et al. 2017).

However, the T_{90} -based classification scheme has significant limitations. The duration of a GRB is not a purely intrinsic property but is instead dependent on the energy band of the detector, the sensitivity thresh-

old, the signal-to-noise (S/N) ratio of the event, and redshift of the source (Y. Qin et al. 2013; O. Bromberg et al. 2013; M. Moss et al. 2022). For instance, T_{90} tends to be longer at lower energies, and bursts with extended soft tails may be misclassified as long GRBs when observed with sensitive instruments like *Swift*-Burst Alert Telescope (BAT). Conversely, low S/N or high background levels can artificially shorten the measured duration. These instrumental dependencies introduce ambiguities, particularly for GRBs near the empirical boundary of $T_{90} \sim 2$ seconds. Moreover, the observed duration distributions of short and long GRBs significantly overlap, further complicating the classification of events near this boundary.

The complexity has only increased with the discovery of more such ambiguous or “hybrid” events that do not conform neatly to the traditional classification scheme. For example, GRB 060614, a long-duration GRB ($T_{90} \sim 100$ sec), showed no accompanying SN emission down to deep optical limits (N. Gehrels et al. 2006; M. Della Valle et al. 2006), challenging the long-GRB/SN association. J. P. U. Fynbo et al. (2006) reported another nearby long-duration GRB 060505, with T_{90} values of 4 sec, that exhibited no SN emission down to limits hundreds of times fainter than SN 1998bw (a prototypical GRB-SN). These nearby “SN-less” GRBs, located in star-forming regions, suggest that not all long GRBs conform to the collapsar model. More recently, long-duration GRBs like GRB 191019A, GRB 211211A, GRB 211227A, and GRB 230307A exhibit signatures (e.g., KN-like emission) consistent with compact binary mergers (J. C. Rastinejad et al. 2022; E. Troja et al. 2022; A. J. Levan et al. 2024; H.-J. Lü et al. 2022; G. Stratta et al. 2025). Conversely, a short-duration burst GRB 200826A, despite $T_{90} \lesssim 2$ sec, is associated with young, star-forming environments and a SN component, suggesting a collapsar origin (T. Ahumada et al. 2021; A. Rossi et al. 2022). These events highlight that duration alone is not a reliable proxy for progenitor type (O. Bromberg et al. 2013; B. Zhang 2025).

These and similar hybrid events also inspired the development of physically-motivated classification systems such as the “Type I (associated with the mergers of compact objects)/ Type II (associated with the collapsars)” scheme (B. Zhang et al. 2009), which incorporates prompt emission, afterglow, host galaxy properties, local environments, and the presence (or absence) of SNe. To overcome the limitations of duration-based classification, the community increasingly employs multiwavelength and multidimensional analyses. Key discriminants include prompt emission properties such as spectral lag (J. P. Norris et al. 2000), and minimum

variability timescale (G. A. MacLachlan et al. 2013), as well as host galaxy properties such as morphology, star formation rate, and metallicity (R. Gupta et al. 2022a; A. S. Fruchter et al. 2006a; W.-f. Fong et al. 2022). Furthermore, machine learning (ML) techniques have been leveraged to integrate these diverse observational parameters into more robust, probabilistic classification frameworks (C. K. Jespersen et al. 2020; S.-Y. Zhu et al. 2024; M. Negro et al. 2025; P. Nuessle et al. 2024; J.-W. Luo et al. 2023).

In this study, we present a comprehensive multiwavelength investigation (classical and ML-based) of GRB 240825A, a long-duration event ($T_{90} \sim 4$ sec) detected by *Fermi*. We examine its prompt emission characteristics (including ML-based classification), afterglow temporal and spectral evolution, and host galaxy properties to establish its classification and physical origin. We used 10.4m *Gran Telescopio Canarias* (GTC) and the Large Binocular Telescope (LBT) telescopes to search for associated SN/KN and decipher the physical origin of GRB 240825A. Despite extensive monitoring, we find no evidence of SN emission to deep limits, reminiscent of GRBs 060505 and 060614. By integrating observations across the electromagnetic spectrum, we aim to place this event within the context of the evolving GRB classification paradigm. Section 2.1 presents the observations and data analysis, Section 3 details the results, and Section 4 discusses the physical interpretation of the results. Conclusions are drawn in Section 5.

2. OBSERVATIONS AND DATA ANALYSIS

2.1. Prompt emission detection

GRB 240825A was detected by the *Fermi* Gamma-ray Burst Monitor (GBM) at 15:53:00 UTC on August 25, 2024 (Fermi GBM Team 2024). The burst was also detected by the *Fermi* Large Area Telescope (LAT), which detected significant high-energy emission above 100 MeV (N. Di Lalla et al. 2024). The *Swift*-BAT independently triggered on GRB 240825A at 15:52:59 UTC, localizing the burst to coordinates RA (J2000) = 22h 58m 12s, Dec (J2000) = +01d 02' 10" with an uncertainty of 3 arcminutes (R. Gupta et al. 2024b). We carried out the temporal analysis of the *Swift*-BAT data of GRB 240825A (see method in R. Gupta et al. 2024a). We utilized *Swift*-BAT data (S. D. Barthelmy et al. 2005) obtained from the HEASARC Data archive⁴⁶. The data, processed with the latest version (6.35.2) of HEASOFT and the latest calibration files, involved re-reducing raw files (Observation

⁴⁶ <https://swift.gsfc.nasa.gov/sdc/>

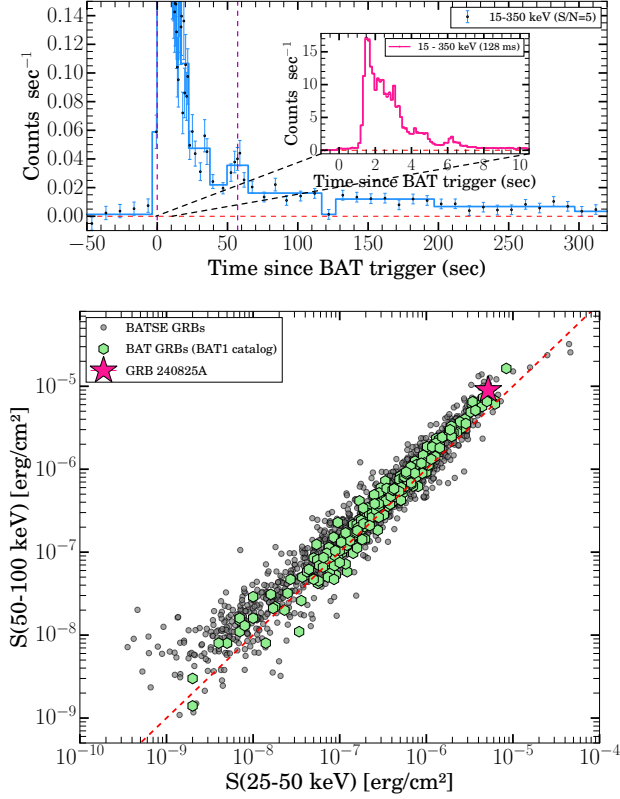


Figure 1. Top: BAT light curve in the 15-350 keV energy range reveals the presence of a faint extended emission post the main burst, observed after employing S/N criteria with 5 or 10-second binning. This helps to delineate possible prolonged emission phases that might be associated with the GRB event. The vertical dashed lines represent a BAT T_{90} duration of 57.20 sec. The inset shows the prompt zoomed light curve of GRB 240825A in the 15-350 keV energy range, observed using the *Swift*-BAT and presented in 128ms time bins, which highlights the burst’s immediate temporal behavior. Bottom: The comparative analysis of GRB 240825A’s fluence (pink star) with other GRBs detected by the BAT and BATSE instruments^a, showing its high fluence ($\sim 10^{-5}$ erg cm $^{-2}$), typically consistent with collapsar GRBs. The red dashed line marks that fluence in the S(50-100 keV) band is equal to fluence in the S(25-50 keV) band.

^a<https://swift.gsfc.nasa.gov/results/batgrbcat/>

ID: 01250617000) using `batbinevt` to generate detector plane images (DPI) and identify hot pixels with `bathotpix`. Mask-weighting and background subtraction were applied via the `batmaskwtevt` pipeline, followed by light curve extraction using `batbinevt`. The mask-weighted light curve (binned at 128 ms in the 15–350 keV band), displayed in Figure 1, shows a bright fast rising exponential decay (FRED)-like main prompt emission pulse, starting at T_0 sec (*Swift*-BAT trigger time), peaking at $T_0 + 1.8$ sec, and ending at $T_0 + 10$ sec. To further probe for any extended emission (EE),

we constructed a light curve with S/N criteria with 5 or 10-second binning, which uncovers faint emission persisting beyond the main emission phase, a feature which has been found in a small number of GRBs and often associated with merger GRBs or hybrid events like GRB 211211A and GRB 230307A (J. P. Norris & J. T. Bonnell 2006; E. Troja et al. 2022; A. J. Levan et al. 2024; S. Dalessi et al. 2025; S. Gupta et al. 2025). This EE, with count rates dropping to ~ 0.01 counts sec $^{-1}$, suggests ongoing energy injection, possibly from a magnetar central engine or prolonged accretion (B. D. Metzger et al. 2008; B. P. Gompertz et al. 2014); however, the exact production channels of this EE are not understood (Q. M. Li et al. 2024). This softer and longer tail emission extends up to $\sim T_0 + 300$ sec with a T_{90} duration of 57.20 ± 8.57 sec (M. J. Moss et al. 2024). We further compared GRB 240825A’s 25–50 keV and 50-100 keV fluence to a sample of *Swift*-BAT and BATSE GRBs, finding its fluence ($\sim 10^{-5}$ erg cm $^{-2}$) to be high (see Figure 1).

2.2. X-ray afterglow

The *Swift* X-Ray Telescope (XRT; D. N. Burrows et al. 2005) initiated observations of the GRB 240825A field at 15:54:22.9 UT, approximately 83.1 seconds after the *Swift*-BAT trigger. The XRT identified a bright, uncatalogued, and fading X-ray source at RA = 22h 58m 16.58s, Dec = +01d 01’ 31.1” (J2000), with a positional uncertainty of 12.3 arcseconds (90% containment). Using 1085 seconds of XRT Photon Counting mode data and two UVOT images, an astrometrically corrected position was determined at RA = 22h 58m 17.28s, Dec = +01d 01’ 36.3” (J2000), with a refined uncertainty of 2.7 arcseconds (90% confidence). This position lies 75 arcseconds from the BAT onboard location, well within the BAT error circle (P. A. Evans et al. 2024). Temporal and spectral data for the X-ray afterglow were retrieved from the *Swift* XRT GRB light curve and spectrum repositories (P. A. Evans et al. 2007, 2009), provided by the UK Swift Science Data Centre⁴⁷. The XRT spectrum in the 0.3–10 keV energy range was fitted with an absorbed power-law model, using both a fixed Galactic absorption model (`phabs`) and a free absorption model (`zphabs`) to constrain contributions from the host galaxy (see A. J. Castro-Tirado et al. 2024; R. Gupta 2023 for detailed methodology).

2.3. Ultra-Violet and optical observations

2.3.1. *Swift*-UVOT

The *Swift*/UVOT (P. W. A. Roming et al. 2005) began observations of the field of GRB 240825A (N. P. M.

⁴⁷ <https://www.swift.ac.uk/>

Kuin et al. 2024) 77 sec after the *Swift*-BAT trigger. The source counts were extracted using a source region of 5 arcsec radius. Background counts were extracted using a 20 arcsec circular region located in a source-free region. The count rates were obtained from the event and image lists using the *Swift* tools `uvotevt1c` and `uvotsource`, respectively. The afterglow count rates were converted to magnitudes using the UVOT photometric zero points (T. S. Poole et al. 2008; A. A. Breeveld et al. 2011). To improve the S/N ratio, the count rates in each filter were binned using $\Delta t/t = 0.2$. The UVOT detector is less sensitive in a few small patches⁴⁸ for which a correction has not yet been determined. Therefore, we determine if the afterglow falls on any of these patches. We find that during the *white*, *u*, and UV filters during the first 1300s, the afterglow does fall on one of these patches. We have therefore excluded the UV data affected by this, but we include *white*, and *u* band data since it provides information on the early time behavior of the afterglow; as such, caution should be used when interpreting the early *white* and *u* band data. For the U-band, the worst-case loss of sensitivity due to these defective patches is -16%, and for the W2 band, the worst case is -40% (with the other two UV bands ranging between those values). The *Swift*/UVOT observations of GRB 240825A, detailed in Table A1 of the appendix, provide AB magnitudes and 3σ upper limits across multiple filters, capturing the temporal evolution of the afterglow from ~ 77 sec to over 425 ks post-burst.

2.3.2. OSN and BOOTES

We conducted optical afterglow observations of GRB 240825A using the 1.5m telescope at the Observatorio de Sierra Nevada (OSN) in Spain and the 0.6m Dolores Pérez-Ramírez robotic telescope (DPRT) at the BOOTES-6 station in South Africa (as part of the BOOTES Global Network, A. J. Castro-Tirado 2023; Y. D. Hu et al. 2023), targeting multiple bands to characterize the afterglow evolution. OSN observations began approximately 8.4 hours ($T-T_0 = 30176$ sec) post-trigger, covering the *B*, *V*, *I*, and *R* bands with exposure times ranging from 300 to 900 seconds. The OSN data were reduced with a custom pipeline that included bias subtraction, flat-field correction using flat frames, and background subtraction to account for varying sky conditions. Aperture photometry, optimized for the afterglow’s point-spread function, was calibrated against nearby Pan-STARRS1 stars to derive AB magnitudes, reported without corrections for Galactic or host ex-

tinction (see Table A2 of the appendix). The afterglow showed a gradual decline across all bands, with *B*-band magnitudes ranging from 21.43 to 22.20, *V*-band from 20.41 to 21.32, *I*-band from 19.83 to 20.06, and *R*-band from 20.22 to 20.52 over the observed period. Complementary *R*-band observations were obtained with the 0.6m BOOTES-6/DPRT starting approximately 2.5 hours ($T-T_0 = 9063$ sec) post-trigger, with exposure times of 600 to 1680 seconds. BOOTES-6 data were reduced with bias and flat-field corrections and initially calibrated to the Vega magnitude system. These magnitudes were converted to the AB system using a zero-point offset of 0.21 mag, yielding values from 19.30 to 20.08, also uncorrected for extinction.

2.3.3. GRB IKI-FuN observations

We continued monitoring the afterglow using a range of telescopes from the IKI Gamma-Ray Burst Follow-up Network (IKI GRB-FuN network (A. Volnova et al. 2021)) and additional facilities. Optical observations were conducted with the 1.5-meter AZT-22 telescope at the Maidanak Astronomical Observatory (MAO), operated by the Ulugh Beg Astronomical Institute in Uzbekistan. Further *R*-band imaging was obtained with the Zeiss-1000 telescope, located at the Special Astrophysical Observatory (SAO) in Russia. Additional observations were carried out using the RC-35 (Kitab) and the Zeiss-1000 telescopes. All our optical data obtained from the IKI GRB-FuN network were processed using NOAO’s IRAF software package⁴⁹. Results of the observations are presented in Table A3 of the appendix.

2.4. Late time Imaging and Spectroscopy: Search for SN and host galaxy

2.4.1. 10.4m GTC spectroscopy observations and redshift determination

We performed spectroscopic observations of the field of GRB 240825A using the Optical System for Imaging and low-Intermediate-Resolution Integrated Spectroscopy (OSIRIS) mounted on the 10.4m GTC, located at the Roque de los Muchachos Observatory, La Palma, Canary Islands. Observations were conducted on 2024 October 9 and 10 under good atmospheric conditions, with airmass ranging from 1.13 to 1.25. We

⁴⁸ https://heasarc.gsfc.nasa.gov/docs/heasarc/caldb/swift/docs/uvot/uvotcaldb_sss_02b.pdf

⁴⁹ IRAF is the Image Reduction and Analysis Facility, a general-purpose software system for the reduction and analysis of astronomical data. IRAF is written and supported by the National Optical Astronomy Observatories (NOAO) in Tucson, Arizona. NOAO is operated by the Association of Universities for Research in Astronomy (AURA), Inc. under cooperative agreement with the National Science Foundation. <https://iraf-community.github.io/>

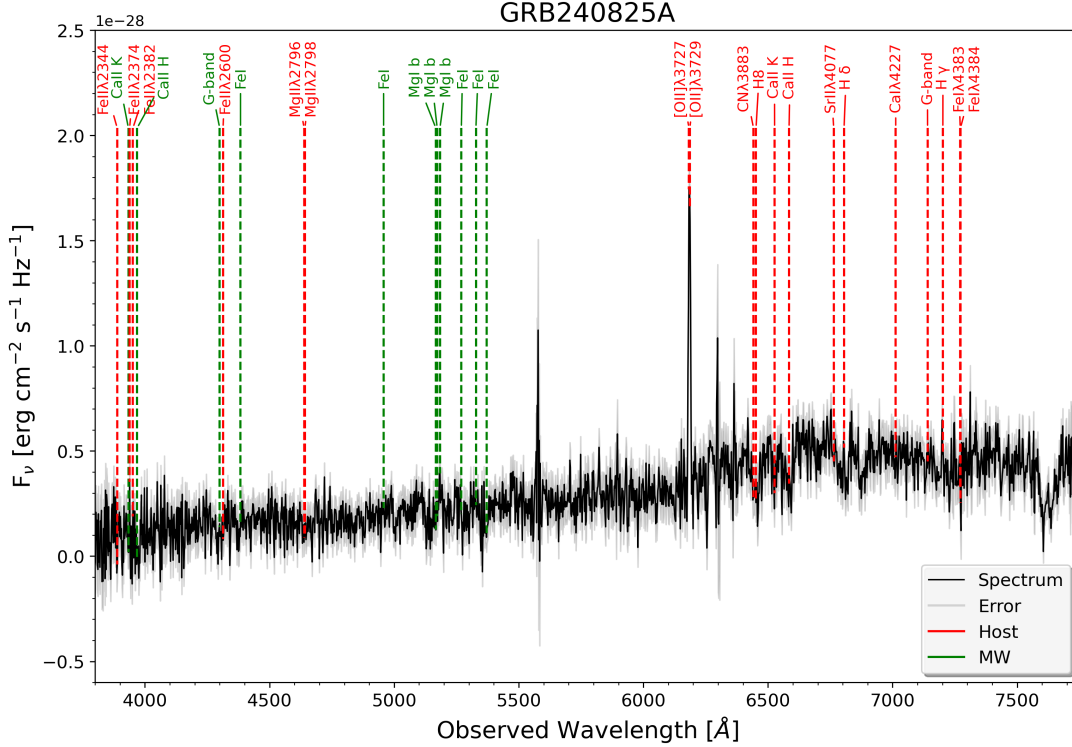


Figure 2. Optical spectrum of the host galaxy of GRB 240825A obtained with the 10.4m GTC. The spectrum (black) is overlaid with the corresponding error spectrum (gray). Features associated with the host galaxy are marked in red, while foreground (Milky Way) features are shown in green. Detected lines include [O II] $\lambda\lambda 3727, 3729$, Ca II H, Ca II K, and several Fe II, Mg II, and Balmer lines, which were used to determine a redshift of $z = 0.659$ for the host galaxy.

used the R1000B grism, which covers the wavelength range of 3630–7500 Å with a spectral resolving power of $R \sim 1000$. On both nights, two exposures of 1200 sec each were obtained targeting the host galaxy of GRB 240825A, as the afterglow was no longer detectable at the time of observation.

Data reduction was performed using standard IRAF routines and complementary python-based tools. The two-dimensional spectroscopic frames were bias-subtracted, flat-field corrected, and cleaned of cosmic rays using the L.A. Cosmic algorithm (P. G. van Dokkum 2001). One-dimensional spectra were extracted using an optimal aperture centered on the galaxy trace after subtracting the background via a low-order polynomial fit to spatial regions adjacent to the target. Wavelength calibration was achieved using comparison arc lamps (Ne, Ar, and Hg), and flux calibration was performed using a spectrophotometric standard star (Feige110) observed on the same nights. Finally, we accounted for slit losses ($\sim 29\%$) scaling the spectrum to the photometric magnitude measured in the r' -band (see detailed methodology (R. Sánchez-Ramírez et al. 2024; Y. D. Hu et al. 2021; R. Gupta et al. 2022b)).

The reduced and calibrated spectrum (Figure 2) exhibits a prominent [O II] $\lambda\lambda 3727, 3729$ emission lines

associated with the host galaxy, as well as several absorption features including Ca II H, Ca II K, the G-band, Ca I $\lambda 4227$, Sr II $\lambda 4077$, CN $\lambda 3883$, and multiple Fe II, Fe I and Mg II lines. These lines were consistently identified across both nights, yielding a redshift measurement of $z = 0.659$ for the host galaxy of GRB 240825A. Our redshift measurement is consistent with the value measured by the VLT equipped with the X-shooter spectrograph (A. Martín-Carrillo et al. 2024). We also noted several foreground (Milky Way) features (see Figure 2) in our spectrum.

2.4.2. 10.4m GTC NIR and optical panchromatic observations

We performed near-infrared (NIR) and optical imaging observations of the host galaxy of GRB 240825A using the 10.4m GTC, equipped with the OSIRIS instrument for optical bands and the Espectrógrafo Multiobjeto Infra-Rojo (EMIR) instrument for NIR bands. Optical imaging was conducted in the g , r , i , and z filters, with exposure times ranging from 400 to 960 seconds, starting approximately 104 days after the GRB trigger ($T-T_0 \sim 104.22$ – 104.26 days), depending on the filter. NIR observations in the J , H , and K bands were obtained with exposure times between 910 and 1260 sec-

Table 1. Host galaxy photometric observations of GRB 240825A.

Instrument/Survey	Filter/Band	T-T ₀ (sec)	Exp. (sec)	AB Mag \pm error
<i>GTC Optical Imaging</i>				
GTC	<i>r</i>	9004750	540	22.45 \pm 0.07
GTC	<i>g</i>	9005075	960	23.76 \pm 0.11
GTC	<i>i</i>	9005502	540	22.03 \pm 0.05
GTC	<i>z</i>	9006216	400	21.63 \pm 0.12
<i>GTC NIR Imaging</i>				
GTC	<i>K</i>	1668561	1260	21.10 \pm 0.06
GTC	<i>J</i>	1671315	910	21.77 \pm 0.10
GTC	<i>H</i>	1673259	1134	21.50 \pm 0.09
GTC	<i>K</i>	2365811	1260	21.14 \pm 0.06
GTC	<i>J</i>	2368461	910	21.81 \pm 0.14
<i>DESI Legacy Surveys (DR10)</i>				
DESI	<i>g</i>	23.607 \pm 0.063
DESI	<i>r</i>	22.463 \pm 0.027
DESI	<i>i</i>	21.875 \pm 0.051
DESI	<i>z</i>	21.627 \pm 0.032
DESI	<i>W1</i>	20.577 \pm 0.102
DESI	<i>W2</i>	21.692 \pm 0.965
DESI	<i>W3</i>	18.141 \pm 1.322
<i>CAHA Optical Imaging</i>				
CAHA	<i>g</i>	2961761	750	23.53 \pm 0.20
CAHA	<i>r</i>	2960729	720	22.71 \pm 0.14
CAHA	<i>i</i>	2959660	720	21.78 \pm 0.15
CAHA	<i>z</i>	2958492	700	21.87 \pm 0.29

NOTE—AB magnitudes are reported without corrections for Galactic or host extinction. For GTC observations, T-T₀ represents the time since the GRB trigger, and Exp. is the exposure time. DESI Legacy Surveys data are from DR10, with no reddening correction applied.

onds, spanning a temporal range of ~ 19.31 to 27.41 days post-trigger. The raw data were processed using the standard pipeline, which included bias subtraction, flat-fielding, and sky subtraction tailored to the varying background levels in each band. Photometry was performed using aperture photometry with a radius optimized for the host’s point-spread function (see [R. Gupta et al. 2021](#) for detailed methodology). Optical AB magnitudes were calibrated against Pan-STARRS standard stars, while NIR magnitudes were calibrated using 2MASS standards, ensuring accurate flux measurements for the GRB 240825A host galaxy. These magnitudes are reported without corrections for Galactic or host extinction (see Table 1).

2.4.3. DESI optical infrared observations

Complementing GTC host observations, we extracted multi-band photometry from the Dark Energy Spec-

troscopic Instrument (DESI) Legacy Surveys Data Release 10 (DR10), covering the *g*, *r*, *i*, *z*, *W1*, *W2*, and *W3* bands, using the survey’s public catalog. For the data analysis of DESI data, we performed aperture photometry with a radius optimized to the host’s point-spread function, calibrated against Pan-STARRS standard stars for optical bands (*g*, *r*, *i*, *z*) and WISE standards for infrared bands (*W1*, *W2*, *W3*). The resulting magnitudes were derived without applying reddening corrections and are summarized in Table 1. We noted that GTC optical measurements remain consistent with DESI values.

2.4.4. 2.2m CAHA optical observations

We also obtained observations with the 2.2 m telescope at the Calar Alto Observatory in Almería, Spain, using the Calar Alto Faint Object Spectrograph (CAFOS). Imaging was performed in the Sloan *g'*, *r'*, *i'*, and *z'* fil-

ters on two epochs: 2024 September 28 and 2024 November 24. However, only the data from the first night were usable due to poor weather conditions during the second epoch. The first observation began at 21:31 UT, corresponding to approximately 34 days post-burst. A faint detection of the GRB host galaxy was noted in the stacked images (see Table 1). The raw data were reduced using standard procedures, including bias subtraction and flat-field correction, followed by image combination and photometric extraction using IRAF routines. Absolute photometric calibration was performed using nearby field stars from the Pan-STARRS1 catalog.

2.4.5. LBT optical observations

We also observed the field of GRB 240825A with the twin Large Binocular Camera (LBCs) mounted on the LBT at Mt. Graham, AZ, USA, in the Sloan r' and z' bands across three epochs (Program: IT-2024B-023, PI E. Maiorano): 2024-09-12 (~ 17.59 days post-burst), 2024-09-28 (~ 33.70 days post-burst), and 2024-11-09 (~ 75.52 days post-burst), with varying exposure times ranging from 30 to 60 minutes per filter to optimize S/N ratios. LBT data were reduced using the standard pipeline (A. Fontana et al. 2014), which includes bias subtraction and flat-fielding, bad pixel and cosmic ray masking, astrometric calibration, and coaddition. We used HOTPANTS-based image subtraction to search for associated SN (see section 4.4). We calibrated the LBT images against Pan-STARRS field stars and uncorrected for foreground Galactic extinction. The host galaxy was clearly detected in both bands.

3. RESULTS

3.1. Prompt emission temporal characteristics

The temporal characteristics of GRB 240825A were analyzed using data from the *Fermi*-GBM in the 50–300 keV energy band to determine its classification within the standard short–long GRB framework. The T_{90} duration, a key discriminator, was calculated from the background-subtracted cumulative count rate profile, precisely identifying the 5% and 95% photon arrival intervals (see Figure 3). This yielded a value of 3.968 ± 0.091 sec measured between 1.024 sec to 4.992 sec after the *Fermi* trigger (T_0). Although this places the burst above the conventional 2-second threshold (instrument dependent, for example, the fourth Fermi Catalog suggested a boundary of 4.2 seconds A. von Kienlin et al. 2020) separating short and long GRBs, the proximity to the boundary complicates a clear-cut classification. Notably, a significantly longer T_{90} of 57.20 ± 8.57 sec was observed by *Swift*-BAT, underscoring how instrumental sensitivity and energy range can affect duration

estimates. Additionally, *Konus-Wind* detected the total duration of main emission of GRB 240825A ~ 2 sec, followed by a weaker emission and softer emission lasts until $\sim T_0 + 25$ sec (D. Frederiks et al. 2024). *AstroSat* Cadmium Zinc Telluride Imager (CZTI) and GECAM-B measured the T_{90} duration of $6.2^{+0.9}_{-0.8}$ sec (J. Joshi et al. 2024), and 5.6 ± 0.3 sec (C.-W. Wang et al. 2024), respectively. These discrepancies highlight the limitations of using a fixed T_{90} criteria and point to the importance of probabilistic classification techniques—such as Gaussian Mixture Models (GMM)—to more robustly distinguish GRB populations across instruments (Z.-B. Zhang et al. 2016).

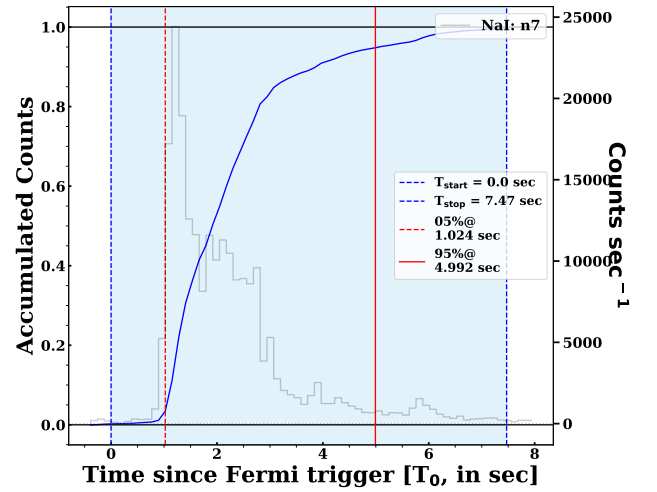


Figure 3. Cumulative count rate and T_{90} calculation for GRB 240825A in *Fermi*-GBM 50–300 keV depicting the cumulative count rate of GRB 240825A as observed by the *Fermi*-GBM in the 50–300 keV energy band, with time measured relative to the GBM trigger. The T_{90} duration, representing the interval containing 90% of the burst’s fluence, is calculated as 3.968 sec, defined by the 5% accumulation level at 1.024 sec (red dashed line) and the 95% level at 4.992 sec (red solid line), with a start time of 0.0 sec and stop time of 7.47 sec (blue dashed lines). The background-subtracted cumulative profile, shown in blue, illustrates the burst’s temporal evolution, with the T_{90} value ~ 2 sec suggesting an ambiguous classification. The background-subtracted GBM light curve is shown in grey.

We analyzed the T_{90} durations⁵⁰ of GRBs jointly observed by BAT (15–350 keV) and GBM (50–300 keV) to investigate their classification into short and long categories (see Figure 4). Using a GMM, we fitted bimodal log-normal distributions to the $\log_{10}(T_{90})$ values for both instruments, capturing the distinct populations

⁵⁰ https://user-web.icecube.wisc.edu/~grbweb_public/

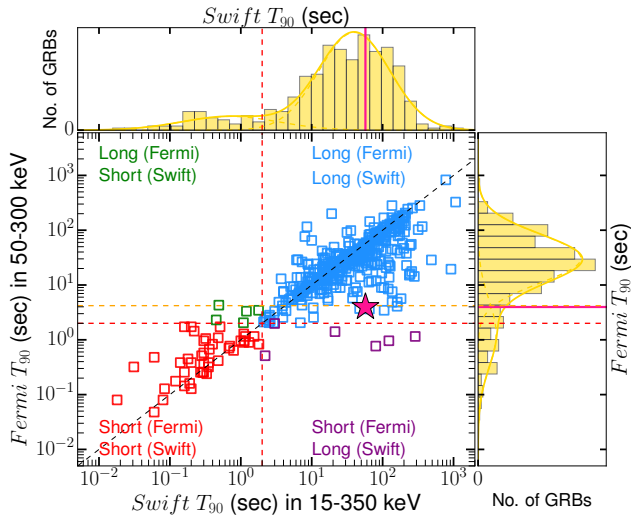


Figure 4. Scatter plot of *Swift* T_{90} versus *Fermi* T_{90} durations for GRBs detected by both instruments. GRBs are classified into four categories: pure long (both $T_{90} > 2$ sec, blue squares), pure short (both $T_{90} \leq 2$ sec, red squares), *Fermi* long–*Swift* short (*Fermi* $T_{90} > 2$ sec, *Swift* $T_{90} < 2$ sec, green squares), and *Swift* long–*Fermi* short (*Swift* $T_{90} > 2$ sec, *Fermi* $T_{90} < 2$ sec, purple squares). GRB 240825A is highlighted in pink star with error bars (*Swift* $T_{90} = 57.20 \pm 8.57$ sec, *Fermi* $T_{90} = 3.968 \pm 0.091$ sec). The dashed black line indicates $y = x$, red dashed lines mark $T_{90} = 2$ sec, and the orange dashed line marks $T_{90} = 4.2$ sec obtained from the fourth *Fermi* Catalog (A. von Kienlin et al. 2020). Histograms along the top and right axes show the logarithmic distributions of *Swift* and *Fermi* T_{90} values, respectively, with fitted bimodal Gaussian Mixture Models (solid gold line) and individual short (dashed gold, lower mean) and long (dashed gold, higher mean) components. Vertical/horizontal lines indicate GRB 240825A’s T_{90} values. The GMM fits reveal distinct short and long GRB populations, with probabilities of GRB 240825A being short calculated as 0.3 % for *Swift* and 48.3 % for *Fermi*.

of short and long GRBs. The matched GRBs were classified into four categories: Pure Long (both $T_{90} > 2$ sec), Pure Short (both $T_{90} \leq 2$ sec), *Fermi* Long–*Swift* Short (*Fermi* > 2 sec, *Swift* ≤ 2 sec), and *Swift* Long–*Fermi* Short (*Swift* > 2 sec, *Fermi* ≤ 2 sec), represented by blue, red, green, and purple markers, respectively. For GRB 240825A, with *Swift* $T_{90} = 57.20 \pm 8.57$ sec and *Fermi* $T_{90} = 3.968 \pm 0.091$ sec, we calculated the probability of being a short GRB using the GMM posterior probabilities, finding a low probability (0.3 %) for *Swift* (consistent with a long GRB) and a high probability (48.3 %) for *Fermi* due to its proximity to the classification boundary. This analysis highlights the differences in T_{90} measurements between instruments, which arise not only from differences in energy sensitivity ranges (*Swift*: 15–350 keV; *Fermi*: 50–300 keV), but also from variations in effective area as a function of energy—both of

which impact detection sensitivity. It also underscores the utility of probabilistic classification for ambiguous cases like GRB 240825A.

3.2. Prompt emission empirical correlations: Classical classification of GRB 240825A

In this section, we classify GRB 240825A using standard prompt emission diagnostics, including the time-integrated peak energy– T_{90} duration (E_p – T_{90}) correlation, the minimum variability timescale– T_{90} duration (t_{mvts} – T_{90}) relation, the Amati relation, and the lag–luminosity correlation. These methods leverage the burst’s temporal and spectral properties to categorize its physical origin.

3.2.1. E_p – T_{90}

The E_p – T_{90} (peak energy–duration) parameter space is a well-established diagnostic tool for distinguishing between merger and collapsar GRBs (R. D. Preece et al. 2000), particularly using *Fermi*–GBM observations (S. Poolakkil et al. 2021; R. Gupta et al. 2024c). In this framework, merger GRBs typically exhibit durations (T_{90}) less than 2 seconds and harder spectra, whereas collapsar GRBs are characterized by longer durations and softer spectra. To investigate the classification of GRB 240825A, we compiled a sample of GRBs from the *Fermi*–GBM catalog⁵¹ and extracted their T_{90} and E_p ($404.81^{+9.02}_{-8.69}$ keV) values (peak energy from time-integrated spectral fits, Gupta et al. in prep). We applied a two-component GMM in the $\log T_{90}$ – $\log E_p$ space to statistically separate the population into merger and collapsar GRBs. This probabilistic approach suggests a refined classification beyond the conventional hard threshold at $T_{90} = 2$ sec, providing a likelihood estimate for each burst. GRB 240825A is located near the boundary between the two populations, with a probability of 28.4% of belonging to the merger GRB class. In Figure 5, we show the position of GRB 240825A on the E_p – T_{90} diagram, along with other GRBs associated with SNe and KNe, for context and comparison.

3.2.2. t_{mvts} – T_{90}

The minimum variability timescale (t_{mvts} or MVT) of a GRB is the shortest timescale over which coherent temporal variations in the light curve can be observed. When the GRB light curve exhibits multiple pulses, the MVT typically corresponds to the timescale of the shortest significant pulse. It has been shown that MVT, in combination with the burst duration (T_{90}), can effectively distinguish between collapsar and merger GRB

⁵¹ <https://heasarc.gsfc.nasa.gov/W3Browse/fermi/fermigbrst.html>

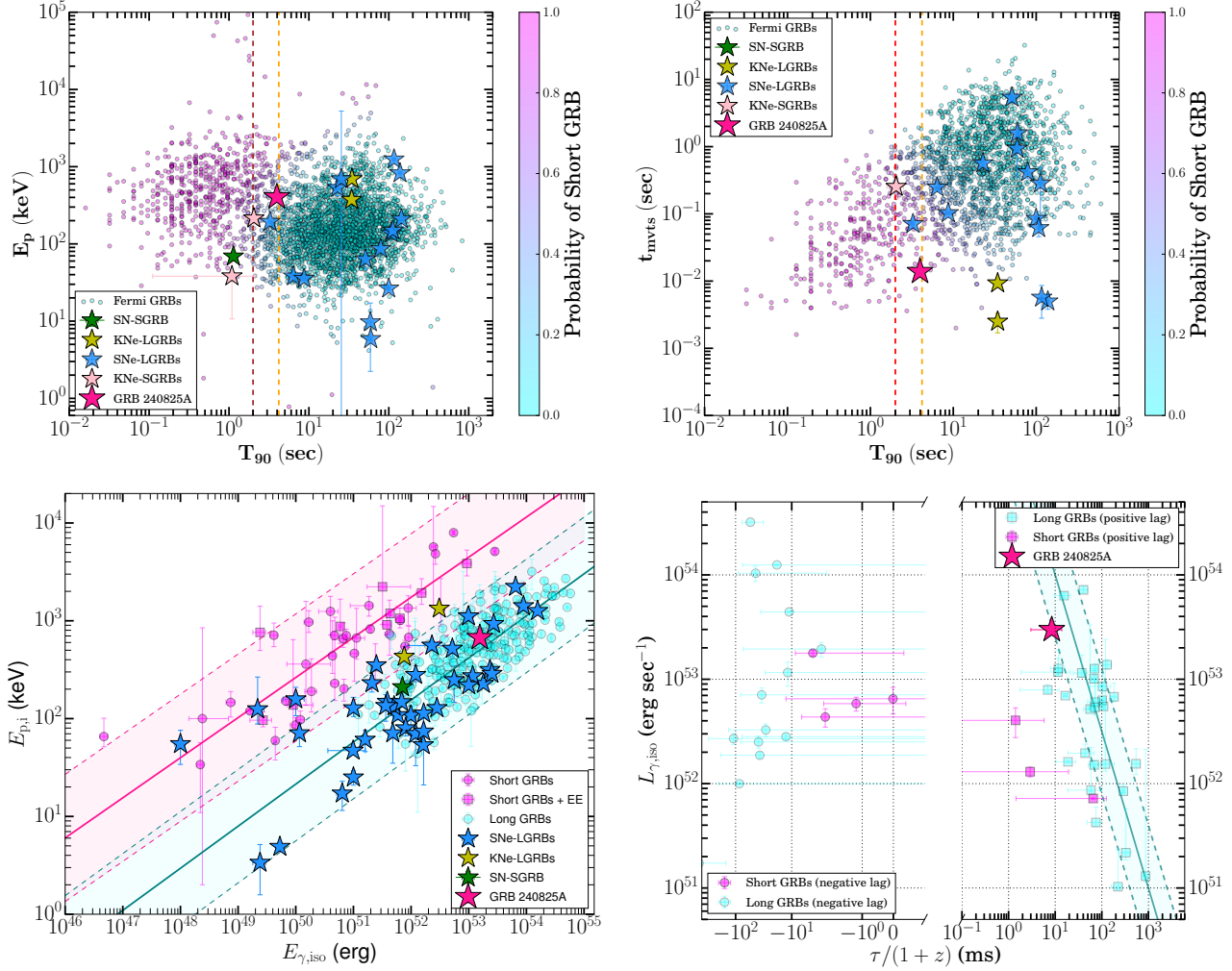


Figure 5. Prompt emission empirical correlations: Top-left: Scatter plot of peak energy (E_p) versus T_{90} duration for a sample of GRBs detected by *Fermi*-GBM. Top-right: Log-log scatter plot of minimum variability timescale (MVT, in seconds) versus T_{90} duration (in seconds) for GRBs detected by *Fermi*-GBM. Red dashed lines mark $T_{90} = 2$ sec, and the orange dashed line marks $T_{90} = 4.2$ sec, respectively. Bottom-left: Log-log scatter plot of peak energy (E_p) versus isotropic-equivalent energy ($E_{\gamma,iso}$) for GRBs obtained from P. Y. Minaev & A. S. Pozanenko (2020). The dashed lines represent the Amati relation for collapsar (cyan) and merger (pink) GRBs (P. Y. Minaev & A. S. Pozanenko 2020). GRB 240825A, with an estimated rest-frame $E_p \approx 671.57$ keV and $E_{\gamma,iso} \approx 1.6 \times 10^{53}$ erg, falls within the collapsar GRB cluster, indicating its classification as a collapsar GRB. Bottom-right: GRB 240825A in the lag-luminosity plane $\log(\tau)$ vs. $\log(L_{iso})$, compared to a sample of *Swift*-BAT GRBs, marginally following the LGRB lag (rest frame)-luminosity relation (T. N. Ukwatta et al. 2010).

populations, offering insight into the compactness and origin of the progenitor systems (e.g., V. Z. Golkhou et al. 2015). We compiled a sample of *Fermi* GRBs with t_{mvts} measurements from V. Z. Golkhou et al. (2015) and additional literature sources (P. Veres et al. 2023), and constructed the t_{mvts} - T_{90} distribution in log-log space. A two-component GMM was applied to this dataset to statistically separate the GRB population. This model allows for probabilistic classification, assigning each burst a likelihood of being associated with the merger GRB class. GRB 240825A was found to have an MVT of 13.8 ± 1.6 ms utilizing GBM observations, as

derived via the wavelet decomposition technique of V. Z. Golkhou et al. (2015). Its location on the t_{mvts} - T_{90} plane (see Figure 5, GRB 240825A along with other KN/SN connected GRBs) places it near the boundary of the merger and collapsar GRB populations, with a calculated merger GRB probability of 95.3%. This statistical analysis supports the interpretation of GRB 240825A as a potential short-duration event, possibly arising from a compact object merger.

Based on the measured t_{mvts} value, and isotropic peak luminosity L_{iso} (Gupta et al. in prep.), we estimated the lower limit of the bulk Lorentz factor (Γ_{min})

and the characteristic emission radius (R_c) using analytical relations obtained from V. Z. Golkhou et al. (2015). These relations connect the minimum variability timescale, isotropic luminosity, and redshift to key physical parameters of the outflow:

$$\Gamma_{\min} \gtrsim 110 \left(\frac{L_{\text{iso}}}{10^{51} \text{ erg/s}} \cdot \frac{1+z}{t_{\text{mvts}}/0.1 \text{ s}} \right)^{1/5} \quad (1)$$

$$R_c \simeq 7.3 \times 10^{13} \left(\frac{L_{\text{iso}}}{10^{51} \text{ erg/s}} \right)^{2/5} \left(\frac{t_{\text{mvts}}/0.1 \text{ s}}{1+z} \right)^{3/5} \quad (2)$$

Applying these relations to GRB 240825A, we obtain a lower limit on the Lorentz factor of $\Gamma_{\min} \gtrsim 565$ and an emission radius of approximately $R_c \simeq 1.60 \times 10^{14}$ cm.

3.2.3. Amati relation

The correlation between the intrinsic peak energy ($E_{p,i}$) and the isotropic-equivalent energy ($E_{\gamma,\text{iso}}$), known as the Amati relation, has long served as an empirical discriminator between collapsar and merger GRBs (L. Amati et al. 2002; Y.-P. Qin & Z.-F. Chen 2013). Collapsar GRBs tend to follow a tight correlation in the $E_{p,i}$ – $E_{\gamma,\text{iso}}$ plane, while merger GRBs, including those with EE, typically fall above this track. To assess the nature of GRB 240825A, we compiled a sample of GRBs from the literature (P. Y. Minaev & A. S. Pozanenko 2020), including merger GRBs with and without EE, collapsar GRBs, and those with confirmed SN or KN associations (J. Yang et al. 2022; X. I. Wang et al. 2022; H. Sun et al. 2025). We then plotted these events in the $E_{p,i}$ – $E_{\gamma,\text{iso}}$ plane and overlaid the best-fit Amati relations for collapsar and merger GRBs based on previous studies (P. Y. Minaev & A. S. Pozanenko 2020). GRB 240825A ($E_{\gamma,\text{iso}} = 1.56 \times 10^{53}$ erg), shown in Figure 5, lies within the 2σ scatter of the collapsar GRB correlation, overlapping with the region occupied by SN-associated long GRBs (SNe-LGRBs). This placement suggests that GRB 240825A is more consistent with the collapsar GRB population in terms of energetics, despite its short-duration characteristics in some diagnostics such as $t_{\text{mvts}}-T_{90}$. Therefore, its classification is complex and potentially indicative of a hybrid event.

3.2.4. Lag-luminosity relation

The lag-luminosity relation, which connects the spectral lag (τ) and the isotropic peak luminosity ($L_{\gamma,\text{iso}}$), has been widely employed as a diagnostic to distinguish between merger and collapsar GRBs (J. P. Norris et al. 2000). Collapsar GRBs typically exhibit positive spectral lags (where higher-energy photons arrive earlier than lower-energy ones) and follow a strong anti-correlation between lag and luminosity (J. P. Norris

2002). In contrast, merger GRBs often show negligible or even negative lags, deviating from the collapsar GRB track in this parameter space (T. N. Ukwatta et al. 2010; M. G. Bernardini et al. 2015). We collected a sample of GRBs with measured lags and luminosities, including both positive and negative lag populations for merger and collapsar GRBs (T. N. Ukwatta et al. 2010; M. G. Bernardini et al. 2015; M. D. Caballero-García et al. 2023).

We calculated the spectral lag for GRB 240825A using the cross-correlation function (CCF) between the 15–25 keV and 50–100 keV light curves from the *Swift*-BAT, focusing on the time interval from 0.67 to 7.58 seconds post-burst. Employing a robust CCF computation with `numpy.correlate` and Monte Carlo error estimation, we fitted the CCF peak with an asymmetric Gaussian model via Markov Chain Monte Carlo (MCMC) sampling, yielding a spectral lag of $\sim 0.014 \pm 0.009$ seconds (68% confidence), indicating that the softer 15–25 keV band lags the harder 50–100 keV band. To contextualize GRB 240825A within the lag-luminosity relation, we estimated its isotropic peak luminosity (L_{iso}) utilizing a peak flux derived from GBM data (Gupta et al. in prep). As shown in Figure 5, GRB 240825A (pink star) marginally satisfy the collapsar GRB lag–luminosity relation, with a rest-frame lag of $\tau/(1+z) \approx 8.44$ ms and $L_{\gamma,\text{iso}} \approx 2.98 \times 10^{53}$ erg sec $^{-1}$. The marginal alignment of GRB 240825A with $\log(L_{\text{iso}}) \propto -\log(\tau)$ relation supports the classification of the burst as a hybrid event, consistent with its prompt emission properties.

3.3. Fermi and ASIM timing analysis of GRB 240825A

GRB 240825A is also detected by the Atmosphere-Space Interactions Monitor (ASIM, T. Neubert et al. 2019). ASIM, installed on the International Space Station (ISS), complements *Fermi* with its High Energy Detector (HED, 0.3–20 MeV) and Low Energy Detector (LED, 50–400 keV), providing enhanced sensitivity to search for quasi-periodic oscillation (QPOs, M. D. Caballero-García et al. 2025). To probe the nature of the central engine powering GRB 240825A, we performed a timing analysis of high-time-resolution light curves from ASIM-HED and *Fermi*-GBM.

We created Power Density Spectra (PDS) for 1.9–3.0 sec (ASIM) and 1.0 to 3.0 sec (*Fermi*) time windows from the two source light curves (ASIM-HED and *Fermi*-GBM) using the `FTOOL-powspec` from the *XRONOS* package of timing tools⁵². The light curves had a time reso-

⁵² <https://heasarc.gsfc.nasa.gov/docs/xanadu/xronos/xronos.html>

Table 2. Power Density Spectra (PDS) timing analysis results of the light curve from GRB 240825A using the $\text{lorentzian+lorentzian+lorentzian+powerlaw}$ function for *Fermi* (upper) and ASIM (lower) data. (T_{start} and T_{stop} have been referred with respect to the *Fermi* reference time ($T_{0,\text{FERMI}}$). The errors given are 1σ .

T_{start} (sec)	T_{stop} (sec)	ν_{QPO1} (Hz)	$\text{FWHM}_{\text{QPO1}}$ (Hz)	N_{QPO1}	ν_{QPO2} (Hz)	$\text{FWHM}_{\text{QPO2}}$ (Hz)	N_{QPO2}	Γ_{P} (Hz)	N_{P} (Hz)	χ^2 (d.o.f.)
1.0	3.0	$6.2^{+0.7}_{-0.06}$	$(1\pm 0.1)\text{E} - 3$	37 ± 30	$19.5^{+1.6}_{-1.0}$	$(1\pm 0.1)\text{E} - 3$	10 ± 8	0 (f)	1.95 ± 0.8	3.5 (5)
1.9	3.0	$6.5^{+0.10}_{-0.7}$	$0.08^{+0.4}_{-0.07}$	61 ± 50	21.7 ± 1.0	$2.1^{+2.1}_{-1.1}$	33 ± 20	0 (f)	1.75 ± 0.8	5.5 (8)

NOTE— ν_{QPO1} , ν_{QPO2} are the frequencies of the QPO features, while $\text{FWHM}_{\text{QPO1}}$, $\text{FWHM}_{\text{QPO2}}$ and N_{QPO1} , N_{QPO2} are its full-width at half-maximum and normalization for both the QPOs, respectively. Γ_{P} and N_{P} represent the high-frequency power-law index and normalization, respectively. χ^2 (d.o.f.): Chi-squared statistic value with degrees of freedom (d.o.f.) in parentheses, indicating the goodness of fit of the model to the data.

lution of 0.016 sec and were divided into 128 points per time interval to calculate the individual PDS that produces the final PDS of each light curve. The PDS were normalized such that their integral gives the squared rms fractional variability, and the expected white noise level was normalized to the level of two (see detailed methodology in *M. D. Caballero-García et al. 2025*). The ASIM-HED and *Fermi*-GBM light curves PDS show peaks at around 6 Hz and 20 Hz (see Figure 6 and Table 2). The significance of these peaks is low, i.e., single-trial significance of $0.3, 1.3\sigma$ for ASIM-HED and with an F-test probability of 0.56, 0.60 for *Fermi*-GBM for the QPOs at 6 Hz and 20 Hz, respectively. While the marginal nature of these features precludes definitive interpretation, we note that high-frequency QPOs in the $\sim 10\text{--}100$ Hz range have been proposed in the literature as a possible signature of magnetar-driven (crustal oscillations) central engines (e.g., *M. D. Caballero-García et al. 2025*; *S. Xiao et al. 2024*) or black hole accretion disks (e.g., instabilities) in collapsar models (*Y. Li et al. 2023*).

3.4. Afterglow temporal and spectral evolution

We conducted the analysis of the optical r-band light curve of GRB 240825A using data from *Y. Cheng et al. (2025)*; *L. Izzo & D. B. Malesani (2024)*; *SVOM/C-GFT Team et al. (2024)*; *A. Martin-Carrillo et al. (2024)*; *R. Brivio et al. (2024)*; *E. Le Floch et al. (2024)*; *B. T. Wang et al. (2024)*; *F. D. Romanov (2024)*, focusing on the first 10^5 seconds to avoid contamination from the host galaxy. The light curve was fitted using a broken power-law function, which effectively observes the temporal evolution of the afterglow. The best-fit parameters are as follows: the temporal decay index before the break, $\alpha_{O1} = -1.60 \pm 0.01$, the temporal decay index after the break, $\alpha_{O2} = -0.94 \pm 0.01$, and the break time, $t_{\text{opt}} = 425.95 \pm 6.70$ seconds. The observed transition from a steeper decay ($\alpha_{O1} = -1.60$) to a shallower decay ($\alpha_{O2} = -0.94$) suggests a significant change in the

emission mechanism. This behavior is consistent with a transition from the reverse shock-dominated phase to the forward shock-dominated phase, as predicted by theoretical models of GRB afterglows (e.g., *R. Sari & T. Piran 1999*). During the early phase, the reverse shock contributes significantly to the optical emission, producing a steeper decline due to the rapid cooling of the shocked ejecta. As the reverse shock fades, the forward shock, driven by the interaction of the GRB jet with the circumburst medium, becomes dominant, resulting in a shallower decay consistent with the synchrotron emission expected in the standard afterglow model (e.g., *B. Zhang & P. Mészáros 2004*). The derived break time of approximately 426 seconds aligns with typical timescales for the reverse-to-forward shock transition observed in other GRBs (e.g., *A. Panaitescu & P. Kumar 2004*). The early steep decay ($\alpha_{O1} = -1.60$) is possibly explained by reverse shock emission in the thin-shell regime. Given the prompt duration $T_{90} = 3.96$ seconds (*Fermi*-GBM), the break time at ~ 426 seconds satisfies the condition $t_{\text{dec}} \gg T_{90}$, indicating the thin-shell case (*C. Wu et al. 2025*). In this regime, the reverse shock is Newtonian and the temporal decay of optical emission (in the slow-cooling regime and for $\nu > \nu_m^{\text{RS}}$) follows $\alpha = -\frac{27p+7}{35}$ (*B. Zhang & S. Kobayashi 2005*). Solving for p , we find $p \approx 1.81$, a physically reasonable value for GRB ejecta and consistent with other GRB reverse shock studies (*R. Gupta et al. 2021*). On the other hand, the shallow post-break decay index ($\alpha_{O2} = -0.94$) is consistent with the expected range for forward shock emission in a constant-density interstellar medium, where the temporal decay index is related to the electron energy distribution index, p , via $\alpha = (3p - 3)/4$ for a slow-cooling regime, i.e., $\nu_{\text{opt}} < \nu_c < \nu_{\text{x-ray}}$ or $\nu_{\text{opt}} < \nu_{\text{x-ray}} < \nu_c$ (*R. Sari et al. 1998*). Assuming $\alpha_{O2} = -0.94$, this implies $p \approx 2.25$ (*C. Wu et al. 2025*), a typical value for GRB afterglows.

We performed a detailed analysis of the X-ray afterglow light curve at 2 keV, utilizing data from the X-ray

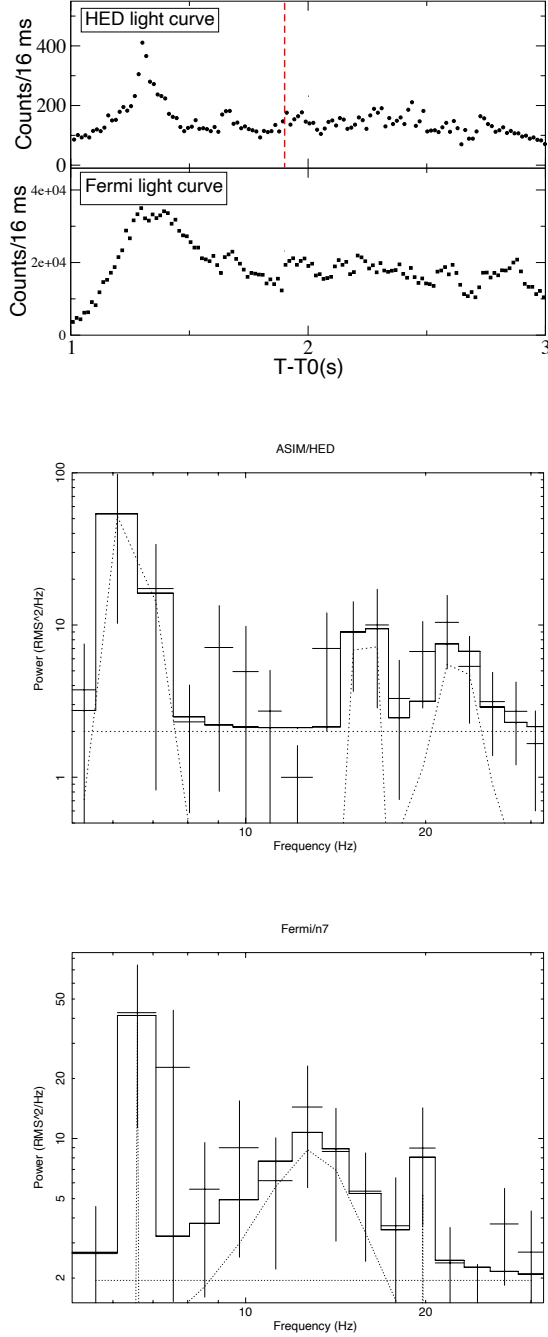


Figure 6. Top: Barycentred ASIM (HED; 0.3-20 MeV) and *Fermi* (GBM; 150 keV-30 MeV) light curves of GRB 240825A showing the time-intervals ($T_0 + 1.9$ to $T_0 + 3.0$ sec and $T_0 + 1.0$ to $T_0 + 3.0$ sec) where the timing analysis was performed. Middle and Bottom: The PDS of the ASIM-HED (0.3-20 MeV) and *Fermi*/NaI-7 (8-800 keV) light curves of GRB 240825A at the time intervals 1.9–3.0 sec and 1.0 – 3.0 sec where T_0 is the *Fermi* trigger time.

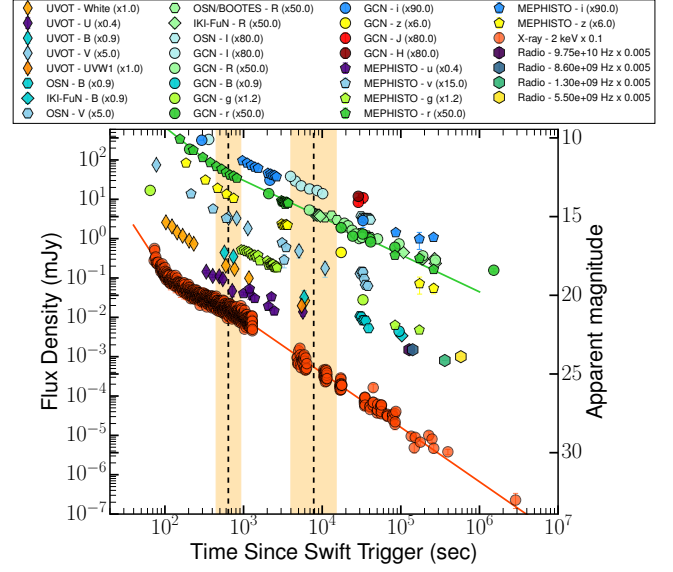


Figure 7. Multi-wavelength light curves of the GRB 240825A afterglow. Solid lines in different colors represent best-fit power-law or broken power-law models applied to the observed data points. Optical data have been corrected for Galactic extinction. Vertical orange shaded bands mark the time intervals used for constructing the spectral energy distributions, with vertical black dashed lines indicating the central times of the SEDs.

Telescope to model its temporal evolution. The light curve was best described by a double broken power-law model having two distinct temporal breaks. The fitted temporal parameters are as follows: the pre-first-break temporal decay index, $\alpha_{X1} = -3.11 \pm 0.25$, the post-first-break temporal decay index, $\alpha_{X2} = -0.97 \pm 0.02$, and the post-second-break temporal decay index, $\alpha_{X3} = -1.38 \pm 0.02$. The first break occurs at $t_{X1} = 115.94 \pm 2.42$ seconds, marking the transition from a steep decay phase to a shallower decline, while the second break at $t_{X2} = 836.65 \pm 40.10$ seconds indicates a further steepening of the decay. We also conducted a spectral analysis of the XRT data during the early steep decay phase ($t < 118$ seconds). The spectrum was modeled with a power-law function, yielding an X-ray spectral index of $\beta = -1.28^{+0.10}_{-0.09}$. This steep decay phase is consistent with high-latitude emission, commonly interpreted as the tail of the prompt GRB emission, where photons from off-axis regions arrive at the observer with a delay due to geometric effects (e.g., [P. Kumar & A. Panaitescu 2000](#)). For non-thermal emission described by a single power-law, the temporal decay index is theoretically related to the spectral index by the relation $\alpha = -2 + \beta$. Given the measured spectral index $\beta = -1.28^{+0.10}_{-0.09}$, the expected temporal decay index is approximately $-3.28^{+0.10}_{-0.09}$, which is in agreement with the observed value

of $\alpha_{X1} = -3.11 \pm 0.25$. This consistency supports the hypothesis that the early steep decay is dominated by the curvature effect of the prompt emission tail.

To investigate the afterglow properties of GRB 240825A, we generated two joint spectral energy distributions (SEDs) using UVOT and XRT data, centered at $T_0 + 640$ s (SED 1) and $T_0 + 7800$ s (SED 2). These SEDs were used to constrain the host galaxy extinction, spectral indices in the X-ray and optical bands, and the location of the synchrotron cooling frequency (ν_c). We employed closure relationships (H. Gao et al. 2013), utilizing temporal and spectral indices in both the interstellar medium (ISM) and wind environments (without energy injection), to further characterize the afterglow properties.

The SEDs were constructed using simultaneous XRT and UVOT observations, covering the energy range from 0.3 to 10 keV and the UV/optical bands, respectively. We followed the methodology described by P. Schady et al. (2007, 2010) to construct the SEDs using UVOT data in the *u*, *b*, and *v* filters for SED 1, and using UVOT data in the *u*, *b*, and *v*, *uvw1*, *uvw2*, and *uvm2* filters for SED 2, respectively. For the XRT data, we extracted spectra in PC mode using the time-sliced spectra option from the *Swift* XRT repository (P. A. Evans et al. 2009). Both SEDs were analyzed using XSPEC (version 12.12.0), following the procedures in P. Schady et al. (2007, 2010). We tested two continuum models: a simple power-law and a broken power-law, with the latter fixing the spectral slope change to $\Delta\beta = 0.5$, consistent with the synchrotron cooling break (R. Sari et al. 1998). Each model incorporated two dust and gas components to account for Galactic and host galaxy extinction and absorption, using the *phabs*, *zphabs*, and *zdst* models in XSPEC. The Galactic components were fixed to the reddening values from D. J. Schlegel et al. (1998) and column density from P. M. W. Kalberla et al. (2005). For the host galaxy, we tested three extinction laws: Small Magellanic Cloud (SMC), Large Magellanic Cloud (LMC), and Milky Way (MW). Additionally, we included the *zigm* component to model absorption due to the Lyman series in the 912–1215 Å rest-frame wavelength range, following the prescription of P. Madau (1995) for optical depth as a function of wavelength and redshift.

The fits were evaluated using the reduced chi-squared relative to degrees of freedom (χ^2/dof), and the null hypothesis probability. For both SEDs, the broken-power law (BKP) provided the best fit (see Table 3), outperforming the single power-law model (POW). Specifically, SED 2 (higher number of UVOT filters) was best described by the broken-power law with LMC extinction

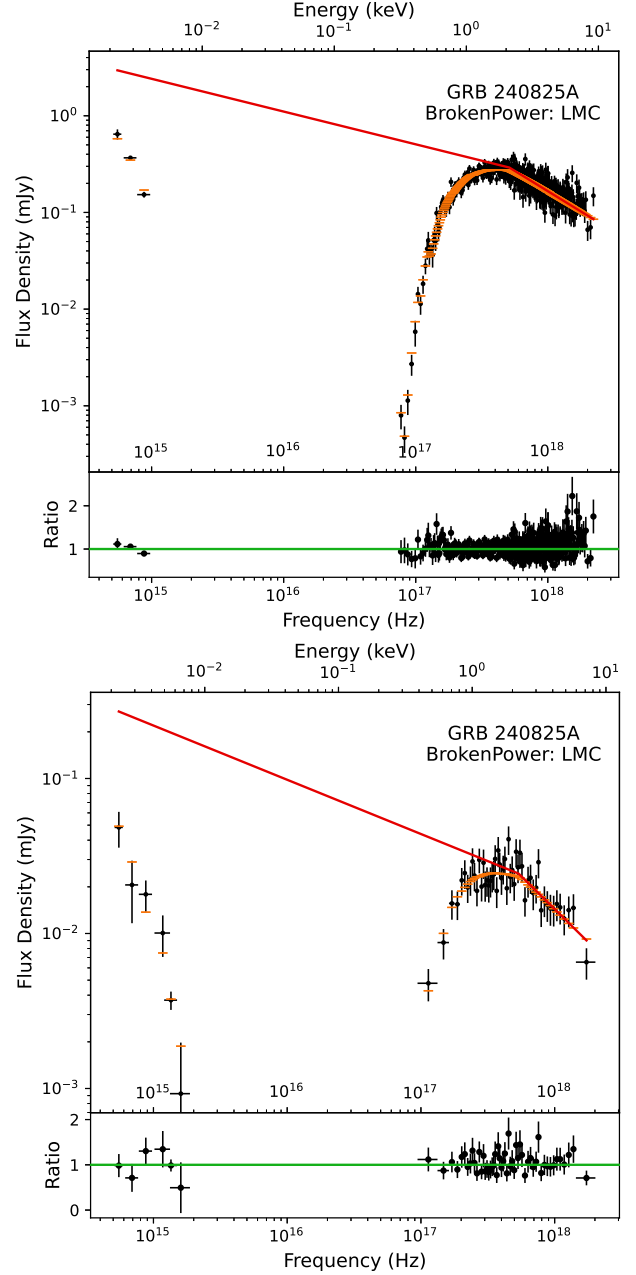


Figure 8. Combined X-ray and UV/optical SEDs for GRB 240825A. Top panel: SED 1, centered at $T_0 + 640$ s, constructed from UVOT data in the *u*, *b*, and *v* filters and XRT data. Bottom panel: SED 2, centered at $T_0 + 7800$ sec, using UVOT data in the *u*, *b*, *v*, *uvw1*, *uvw2*, and *uvm2* filters and XRT data. Both SEDs were optimally fitted with a broken power-law (BKP) model, with the Large Magellanic Cloud extinction law providing the best fit. Observed and model data points, affected by host galaxy absorption and extinction, are shown in black and orange, respectively. The solid red line represents the best-fit model corrected for absorption and extinction. The lower sub-panel in each figure displays the data-to-model ratio, demonstrating the quality of the fit across the energy range.

Table 3. Results of simultaneous UV/optical and X-ray spectral fits for GRB 240825A, using SMC, LMC, and MW extinction laws with power-law (POW) and broken power-law (BKP) continuum models. For the broken power-law, the second spectral index is fixed as $\beta_2 = \beta + 0.5$. Columns list the spectral index (β), host galaxy column density (N_H), color excess ($E(B - V)$), break energy (E_{bk}) for broken power-law models, χ^2 , degrees of freedom (dof), and null hypothesis probability.

SED	Model	Dust	β	N_H (10^{22} cm^{-2})	$E(B - V)$ (mag)	E_{bk} (keV)	χ^2 (dof)	Null Hypothesis Probability
SED 1 ($T_0 + 640 \text{ sec}$)								
640 s	POW	MW	1.61 ± 0.02	1.17 ± 0.04	0.58 ± 0.02	–	562.15 (458)	6.15e-04
640 s	POW	LMC	1.62 ± 0.02	1.19 ± 0.04	0.57 ± 0.02	–	549.20 (458)	2.15e-03
640 s	POW	SMC	1.62 ± 0.02	1.19 ± 0.04	0.59 ± 0.02	–	549.70 (458)	2.05e-03
640 s	BKP	MW	1.33 ± 0.02	1.00 ± 0.04	0.30 ± 0.02	2.08 ± 0.11	464.85 (457)	3.90e-01
640 s	BKP	LMC	1.34 ± 0.03	1.00 ± 0.04	0.30 ± 0.02	2.10 ± 0.12	466.62 (457)	3.68e-01
640 s	BKP	SMC	1.33 ± 0.03	1.00 ± 0.04	0.31 ± 0.02	2.09 ± 0.12	465.62 (457)	3.80e-01
SED 2 ($T_0 + 7800 \text{ sec}$)								
7800 s	POW	MW	1.59 ± 0.04	0.81 ± 0.11	0.61 ± 0.04	–	59.09 (55)	3.29e-01
7800 s	POW	LMC	1.46 ± 0.03	0.63 ± 0.09	0.37 ± 0.03	–	64.16 (55)	1.86e-01
7800 s	POW	SMC	1.37 ± 0.03	0.52 ± 0.08	0.27 ± 0.02	–	76.03 (55)	0.32e-01
7800 s	BKP	MW	1.48 ± 0.08	0.79 ± 0.12	0.53 ± 0.06	2.79 ± 0.62	50.11 (54)	6.25e-01
7800 s	BKP	LMC	1.35 ± 0.05	0.69 ± 0.10	0.31 ± 0.03	2.22 ± 0.30	42.26 (54)	8.77e-01
7800 s	BKP	SMC	1.27 ± 0.04	0.61 ± 0.10	0.23 ± 0.02	2.08 ± 0.28	42.89 (54)	8.62e-01

(SMC model also provides equally good fit, but we prefer LMC), with a reduced chi-squared of 0.78 and a null hypothesis probability of 0.88, indicating a statistically robust description of the data. This model suggests a spectral break at an energy of approximately 2.22 keV, with a pre-break photon index of 1.35 and a post-break index constrained by the data. Given this result, we adopted the LMC extinction law for SED 1 as well, where it also yielded the best fit (reduced chi-squared = 1.0211, null hypothesis probability = 0.3677), with a break at ~ 2.10 keV and a pre-break photon index of 1.34. While SED 2 clearly favored LMC over MW and SMC due to its inclusion of more UVOT filters, SED 1's extinction preference was less distinct, likely due to fewer UVOT filters, though LMC remained consistent with the data. The dominance of the broken-power law and the preference for LMC or SMC-like extinction suggest synchrotron emission in a low-metallicity environment, with stable spectral characteristics across the two epochs.

We conducted the analysis of the late-time afterglow of GRB 240825A, utilizing joint X-ray and optical observations, the temporal and spectral evolution obtained through SED fitting, and closure relation analysis. The SED, constructed from simultaneous X-ray and optical data, reveals a break at $E_{\text{break}} = 2.22 \pm 0.30$ keV within the X-ray band (see Figure 8), consistent with the cooling frequency ν_c in a synchrotron emission framework. Assuming a slow-cooling regime in a constant-density interstellar medium (ISM) and an electron energy distribution index $p > 2$ (indicative of a softer, non-thermal

power-law distribution of shock-accelerated electrons), we explored following spectral regime based on the relative positions of the optical frequency (ν_{opt}), X-ray frequency ($\nu_{\text{x-ray}}$), and cooling frequency (ν_c):

$\nu_{\text{opt}} < \nu_c < \nu_{\text{x-ray}}$: The optical band lies below ν_c , and the X-ray band lies above, giving $\alpha_{\text{opt}} = \frac{3(p-1)}{4}$, $\alpha_{\text{x-ray}} = \frac{3p-2}{4}$, $\beta_{\text{opt}} = \frac{p-1}{2}$, and $\beta_{\text{x-ray}} = \frac{p}{2}$.

Using the derived electron distribution index $p \approx 2.25$ from the optical afterglow, we calculated the expected X-ray temporal decay index for the ISM model. For the second regime ($\nu_{\text{opt}} < \nu_c < \nu_{\text{x-ray}}$), the expected $\alpha_{\text{x-ray}} = \frac{3p-2}{4} = \frac{3(2.25)-2}{4} \approx 1.19$, which is marginally consistent with the observed $\alpha_{X3} = -1.38 \pm 0.02$, suggesting this regime is plausible but not a perfect fit.

We also tested closure relations for a wind-like medium, characterized by a density profile $\rho \propto r^{-2}$. For the optical afterglow, the late-time decay index $\alpha_{O2} = -0.94 \pm 0.01$ and spectral index $\beta_{\text{opt}} \approx 0.35$ are consistent with a slow-cooling forward shock below ν_c ($\nu_m < \nu_{\text{opt}} < \nu_c$), where $\alpha = \frac{3p-1}{4}$ and $\beta = \frac{p-1}{2}$. Using $\beta_{\text{opt}} \approx 0.35$, we find $p \approx 1.7$. For the X-ray afterglow, with $\alpha_{X3} = -1.38 \pm 0.02$ and $\beta_{\text{x-ray}} \approx 0.85$, we tested the regime above ν_c ($\nu_{\text{x-ray}} > \nu_c$), where $\alpha = \frac{3p-2}{4}$ and $\beta = \frac{p}{2}$. Using $p \approx 1.7$, we calculate $\alpha \approx \frac{3(1.70)-2}{4} \approx 0.78$, which are inconsistent with the observed $\alpha_{X3} = -1.38$. The observed break at $E_{\text{break}} \approx 2.2$ keV supports the $\nu_{\text{opt}} < \nu_c < \nu_{\text{x-ray}}$ regime in the ISM model, but the inconsistencies in α across both bands indicate that no single standard synchrotron closure relation fully describes both bands simultaneously. This tension may indicate

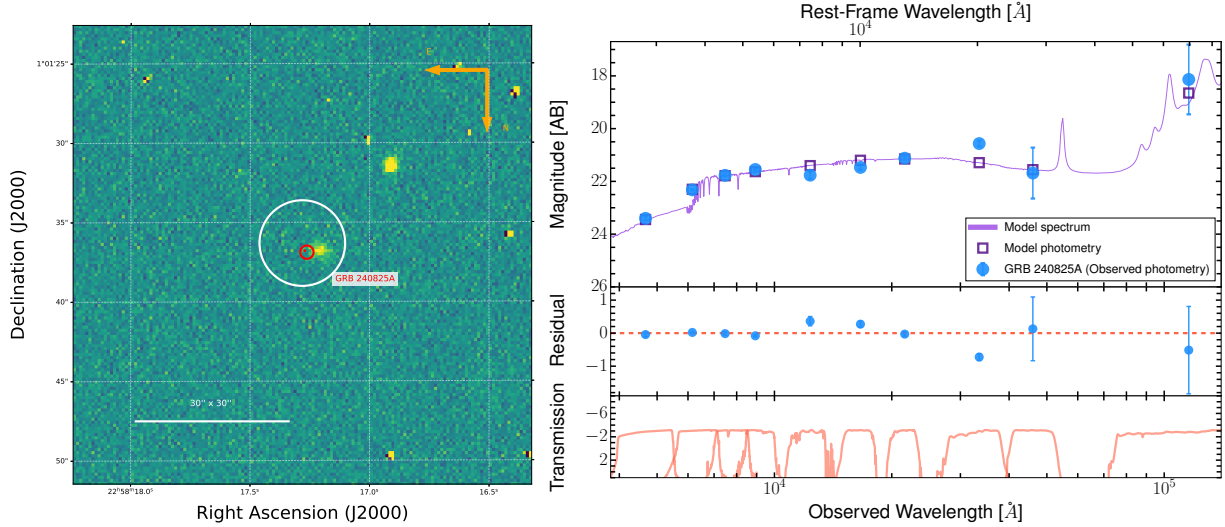


Figure 9. Left: H-band finding chart ($30'' \times 30''$) obtained using 10.4 m GTC. The UVOT and XRT uncertainty error circles are marked using red and white colors, respectively. The host galaxy of GRB 240825A is clearly visible, close to the afterglow position. Right: Best-fit spectral energy distribution model for the host galaxy of GRB 240825A using *Prospector*, constructed from broadband photometry spanning optical to mid-infrared wavelengths. The sky blue points represent observed photometry from 10.4 m GTC and DESI Legacy Surveys in the g , r , i , z , J , H , K , $W1$, $W2$, and $W3$ bands, uncorrected for the host extinction. The light blue line shows the best-fit model from *Prospector*, with the shaded region indicating the 1σ uncertainty. The rest-frame wavelength is plotted on the top x-axis, extending to approximately 10^5 Å. Residuals between the observed and modeled fluxes are shown in the middle panel, with a dashed line marking the residuals equal to zero. The transmission of each filter is shown in the lower panel.

a complex afterglow evolution, potentially driven by a two-component jet model (e.g., a narrow core and wider cocoon), a wavelength-dependent model, or a transition in the external medium density profile (e.g., from wind to ISM). Alternatively, the circumburst environment may follow a non-trivial density profile, parameterized as $\rho \propto r^{-k}$ with $0 \leq k \leq 2$, which has been shown to affect the temporal and spectral indices (H. Gao et al. 2013). Energy injection or evolving microphysical parameters (e.g., magnetic field amplification) could also steepen the X-ray decay beyond standard predictions (e.g., B. Zhang et al. 2006; K. Misra et al. 2021). Further multiwavelength observations, including radio and high-energy data, are essential to refine these models and elucidate the physical processes governing the afterglow of GRB 240825A.

3.5. Host galaxy properties

Host galaxy properties provide crucial context for distinguishing between collapsar and merger GRBs, offering insights into their progenitor systems. Collapsar GRBs are predominantly found in star-forming galaxies with low metallicities, consistent with the collapsar model in which massive, rapidly rotating stars end their lives in core-collapse events (A. S. Fruchter et al. 2006b; S. Savaglio et al. 2009). These galaxies often exhibit high specific star formation rates and young stellar populations. In contrast, merger GRBs are found in a

broader range of galactic environments, including both early-type (elliptical) and late-type galaxies, with generally older stellar populations and lower star formation rates (E. Berger 2014b; W. Fong et al. 2013). Some merger GRBs are located in the outskirts of their host galaxies or even appear to be hostless, suggesting significant natal kicks and long delay times between formation and merger of compact object binaries (W. Fong et al. 2010). The diversity in host environments thus supports a binary neutron star or neutron star–black hole merger origin for merger GRBs, while collapsar GRBs trace regions of recent massive star formation. In our analysis, we utilize the host galaxy properties to probe the likely progenitor and classify the physical origin of GRB 240825A.

3.5.1. Host SED analysis

We conducted a comprehensive spectral energy distribution (SED) analysis of the host galaxy of GRB 240825A using the *Prospector* SED fitting code to characterize its stellar population and star formation properties. The SED was constructed from broadband photometry spanning optical to mid-infrared wavelengths, including deep imaging from the 10.4 m GTC in the g , r , i , z , J , H , and K bands, and archival data from the DESI Legacy Surveys in the $W1$, $W2$, and $W3$ bands. Photometric data were corrected for galactic extinction using the E. F. Schlafly & D. P. Finkbeiner

(2011) dust maps, while internal dust attenuation was modeled within *Prospector*. The SED was fitted in the rest frame at the host's redshift ($z = 0.659$), with rest-frame wavelengths extending from optical to $\sim 10^5$ Å, as shown in Figure 9.

We employed the *parametric_sfh* model⁵³ in *Prospector*, assuming a delayed- τ star formation history ($\text{SFR}(t) \propto (t/\tau^2)e^{-t/\tau}$), and sampled the parameter space using Markov Chain Monte Carlo (MCMC) methods. Key parameters included stellar mass (M_*), metallicity (Z), galaxy age (t_{age}), dust attenuation (A_V), and the e-folding time (τ), which characterizes the exponential decline of the star formation rate. The corner plot (see Figure A1 of the appendix) displays posterior distributions for parameters such as $\log(\text{mass})$ and $\log(\tau)$, indicating robust constraints. The best-fit model yields a stellar mass of $\log(M_*/M_\odot) \approx 10.62$ and a star formation timescale of $\tau \approx 1.07$ Gyr. The star formation rate (SFR), derived from the model, is approximately $1.95 M_\odot \text{yr}^{-1}$, consistent with an extended star formation history for a massive galaxy. The best-fit spectrum matches the observed photometry with low residuals (Figure 9), validating the model's accuracy.

3.5.2. Comparative analysis of GRB 240825A host galaxy properties with Collapsar and Merger GRB hosts

Using the *Prospector* tool, we derived the stellar mass, star formation rate (SFR), and specific star formation rate (sSFR) of the host galaxy of GRB 240825A to contextualize its properties relative to other GRB hosts and infer its progenitor environment. The host's stellar mass is constrained to $\log M/M_\odot = 10.62^{+0.24}_{-0.19}$, with an SFR of $1.95 M_\odot \text{yr}^{-1}$, yielding an sSFR of $\text{sSFR}/\text{Gyr}^{-1} = 4.64 \times 10^{-2} \text{ Gyr}^{-1}$, $A_V = 1.73^{+0.24}_{-0.19}$ mag, consistent with a moderately star-forming dusty galaxy at its redshift ($z = 0.659$). Comparative analysis with a diverse sample of GRB hosts, including Type II GRBs (typically associated with massive star collapse) and Type I GRBs (often linked to compact object mergers), positions GRB 240825A's host below the main sequence of star-forming galaxies in the $\log \text{SFR}$ versus $\log M/M_\odot$ plane (see Figure 10). This placement, at $\log \text{SFR} \approx 0.29$ and $\log \text{sSFR} \approx -1.33$, indicates a modest SFR for its substantial stellar mass, commonly observed in collapsar GRB hosts (e.g., S. Savaglio et al. 2009; L. K. Hunt et al. 2014; K. Taggart & D. A. Perley 2021; J. Japelj et al. 2016). The sSFR, lower than the median for collapsar GRB hosts, aligns more closely with merger GRB hosts (E. Berger 2014b); however, a few GRB hosts of LGRBs have also been observed with such low sSFR. This sug-

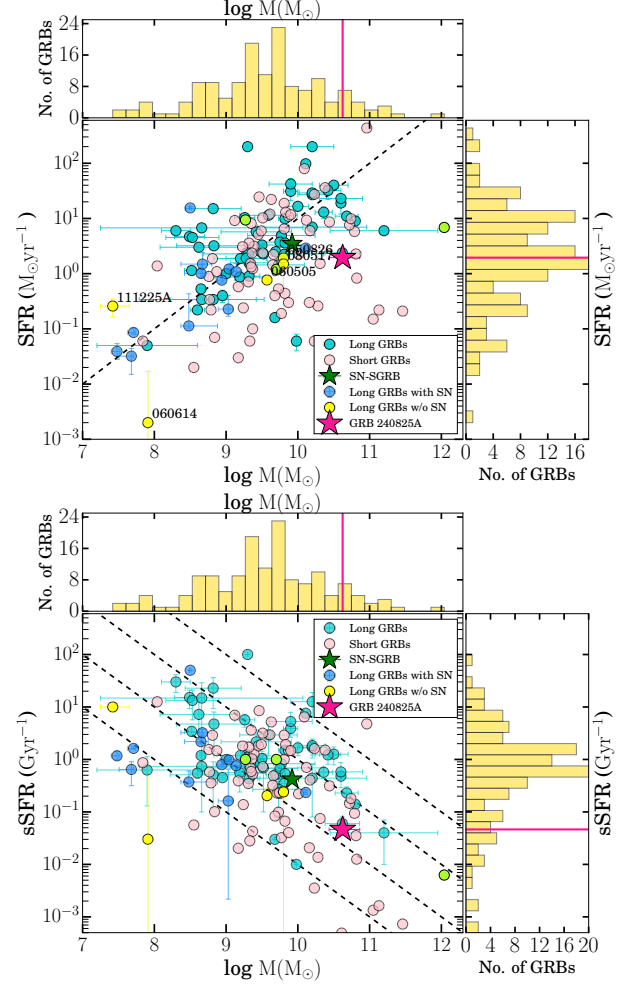


Figure 10. This figure illustrates the host galaxy properties of GRB 240825A compared to collapsar (depicted with cyan circles) and merger (depicted with pink circles) GRBs taken from S. Savaglio et al. (2006, 2009); K. Taggart & D. A. Perley (2021); A. E. Nugent et al. (2022); R. Gupta et al. (2022a), providing insight into its environmental characteristics. Top Panel: Stellar mass ($\log M/M_\odot$) versus star formation rate ($\text{SFR}/M_\odot \text{yr}^{-1}$), with GRB 240825A marked as a pink star at $\log M/M_\odot \approx 10.62$ and $\text{SFR} \approx 1.95 M_\odot \text{yr}^{-1}$. Histograms of stellar mass and SFR are shown along the top X-axis and right Y-axis, respectively. A dashed black line denotes a specific star formation rate of 1 Gyr^{-1} , representing the main sequence of star-forming galaxies. Bottom Panel: Stellar mass versus specific star formation rate ($\text{sSFR}/\text{yr}^{-1}$), with histograms of stellar mass and sSFR along the top X-axis and right Y-axis, respectively. In both panels, GRB 240825A's host galaxy is highlighted with a pink star, and its position in the histograms is marked by vertical pink lines. Dashed black lines denote star formation rates (sSFR) of 0.1, 1, 10, 100 $M_\odot \text{yr}^{-1}$. The host of GRB 240825A falls below the main sequence in the mass-SFR plot, suggesting a lower sSFR than typical star-forming galaxies, a trait more consistent with merger GRB hosts than the typically higher sSFR seen in collapsar GRB hosts.

⁵³ <https://prospect.readthedocs.io/en/latest/sfhs.html>

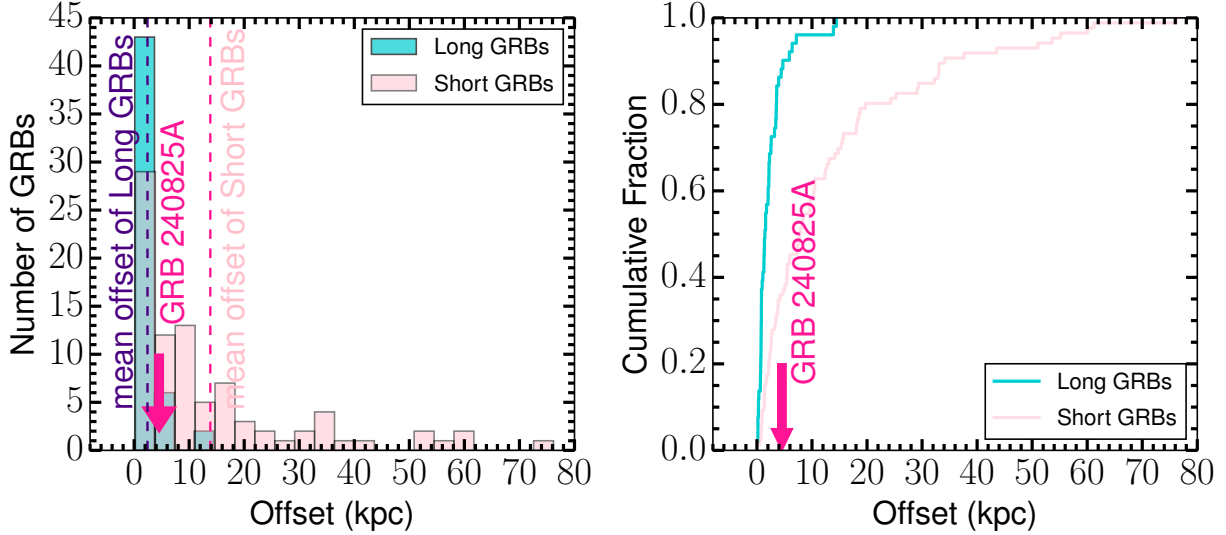


Figure 11. Left panel: Histogram of physical offsets (in kpc) for collapsar GRBs (cyan) and merger GRBs (light pink), with the mean offset of GRB 240825A (4.54 kpc) marked by a pink arrow. The mean offsets are 2.426 kpc for collapsar GRBs and 13.838 kpc for merger GRBs, with medians of 1.451 kpc and 7.820 kpc, respectively. Right panel: Cumulative fraction of offsets for collapsar GRBs (cyan) and merger GRBs (light pink), with the position of GRB 240825A (4.54 kpc) indicated by a pink arrow. The offset of GRB 240825A, derived from the host position (RA 22:58:17.23, Dec +01:01:36.48) and VLA position (RA 22:58:17.27, Dec +01:01:36.78) at ($z = 0.659$), suggests an intermediate location between typical collapsar and merger GRB populations, hinting at a potential off-axis massive star progenitor scenario.

gests that GRB 240825A’s progenitor may have emerged in a relatively quiescent environment or a distinct formation mechanism compared to typical collapsar GRB progenitors.

These properties—a relatively massive host, subsolar metallicity, and ongoing star formation—are consistent with typical hosts of long-duration GRBs, as noted in studies like [S. Savaglio et al. \(2009\)](#); [R. Gupta et al. \(2022a\)](#). On the other hand, low sSFR hints a possible merger progenitor origin for GRB 240825A.

3.5.3. Host offset and progenitor implications

The projected physical offset between a GRB afterglow and its host galaxy center provides key insights into the nature of its progenitor system. Collapsar GRBs, believed to originate from the collapse of massive stars, are typically found near the star-forming regions of their hosts and thus exhibit smaller offsets. In contrast, merger GRBs, which are thought to result from compact object mergers, often show larger offsets due to natal kicks and long inspiral times (e.g., [W. Fong et al. 2010](#); [E. Berger 2014b](#)). For GRB 240825A, we derive a projected offset of 4.54 kpc based on the angular separation (0.64 arcseconds) between the VLA-detected afterglow position (RA: 22:58:17.27, Dec: +01:01:36.78) and the host galaxy centroid (RA: 22:58:17.23, Dec: +01:01:36.48). In the context of known GRB populations ([P. K. Blanchard et al. 2016](#); [W.-f. Fong et al. 2022](#)), this offset lies between the typical ranges

for merger and collapsar GRBs. Specifically, collapsar GRBs have a mean (median) offset of 2.43 kpc (1.45 kpc), while merger GRBs exhibit significantly larger mean (median) values of 13.84 kpc (7.82 kpc). Figure 11 shows the offset distribution for both GRB classes and the cumulative distribution comparison. The offset of GRB 240825A is more consistent with the upper tail of collapsar GRB offsets, suggesting a probable massive star origin while not excluding a compact binary merger scenario entirely. This intermediate offset highlights the importance of multi-wavelength and multi-parameter classification for robust GRB progenitor identification.

4. DISCUSSION

4.1. Rest-frame Energetics: $E_{\gamma, \text{iso}}$ and $E_{\text{p}, i}$

Understanding the redshift evolution of prompt emission properties such as the isotropic-equivalent gamma-ray energy ($E_{\gamma, \text{iso}}$) and rest-frame peak energy ($E_{\text{p}, i}$) is critical for classifying GRBs and probing their progenitor systems. Collapsar GRBs, associated with collapsars, typically exhibit higher $E_{\gamma, \text{iso}}$ and lower $E_{\text{p}, i}$ values over a broad redshift range, while merger GRBs, often originating from compact binary mergers, tend to occupy a distinct region in this parameter space with lower energetics and higher spectral hardness. We compared the location of GRB 240825A in the $E_{\gamma, \text{iso}}$ vs $(1+z)$ and $E_{\text{p}, i}$ vs $(1+z)$ planes against a well-classified

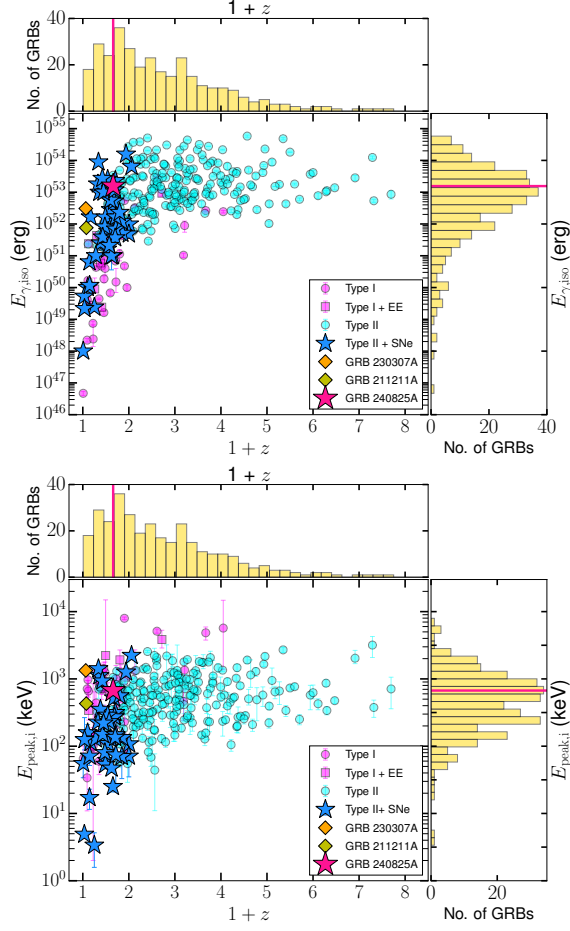


Figure 12. Top panel: Isotropic-equivalent energy $E_{\gamma, \text{iso}}$ plotted against redshift for a sample of classified GRBs from P. Y. Minaev & A. S. Pozanenko (2020). GRB 240825A (pink star) is shown alongside GRB 211211A and GRB 230307A for comparison. GRB 240825A lies close to the classical collapsar GRB region. Merger GRBs (Type I), merger GRBs with extended emission (Type I+EE), collapsar GRBs (Type II), and collapsar GRBs with confirmed SNe (Type II+SNe) are color-coded. Bottom panel: Rest-frame spectral peak energy $E_{p, i}$ as a function of redshift, with the same GRB sample. GRB 240825A (pink star) appears harder than typical collapsar GRBs but softer than the hardest merger GRBs $z=0.659$. Its position in the $E_{\gamma, \text{iso}}-(1+z)$ and $E_{p, i}-(1+z)$ planes suggests its classification as a possible hybrid event and needs further diagnostics.

GRB population from P. Y. Minaev & A. S. Pozanenko (2020); H. Sun et al. (2025); J. Yang et al. (2022). As shown in Figure 12, GRB 240825A falls in an intermediate region—more energetic than typical merger GRBs, yet harder than classical collapsar GRBs at $z=0.659$ —consistent with the distribution of hybrid events such as GRB 211211A and GRB 230307A. Its energetics ($E_{\gamma, \text{iso}}$ and $E_{p, i}$) are thus not reconciled with a purely merger or collapsar classification, further motivating a multi-

dimensional diagnostic approach to understanding its progenitor nature.

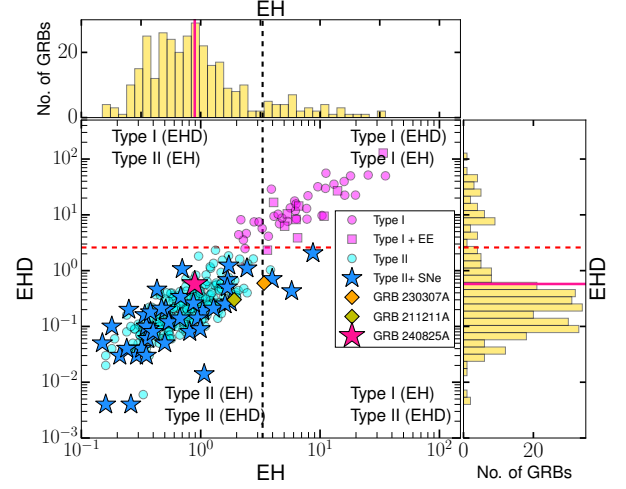


Figure 13. EHD vs. EH distribution of gamma-ray bursts from P. Y. Minaev & A. S. Pozanenko (2020), showing the distinction between Type I, Type II, those with extended emission (Type I+EE), and Type II+SNe. GRB 240825A (pink star) is shown alongside GRB 211211A and GRB 230307A for comparison. GRB 240825A lies close to the classical type II GRBs region. The vertical black and red horizontal dashed lines show $\text{EHD} = \text{EH}$, respectively.

4.2. GRB 240825A: New classification schemes and possible progenitor

In recent times, some authors have proposed physically motivated classifications of GRBs to complement the traditional duration-based scheme. For example, P. Y. Minaev & A. S. Pozanenko (2020) introduced a robust classification scheme based on two parameters: energy-hardness (EH) and energy-hardness-duration (EHD). These parameters provide a valuable diagnostic tool for GRB classification, especially when traditional duration- or spectral-based criteria prove ambiguous. In the EH–EHD parameter space, collapsar GRBs (Type II) tend to occupy regions with low EH–EHD, while merger GRBs (Type I) cluster at higher values of both parameters. In Figure 13, we compare GRB 240825A against this framework. Our analysis places the burst in a region overlapping with type II GRBs (see Figure 13). We also analyzed GRB 211211A and GRB 230307A (long merger events, H. Sun et al. 2025; J. Yang et al. 2022) following the same parameter spaces and noted that GRB 211211A is consistent with type II GRBs; however, for GRB 230307A, the EH parameter suggests that the burst possibly belongs to type I GRBs.

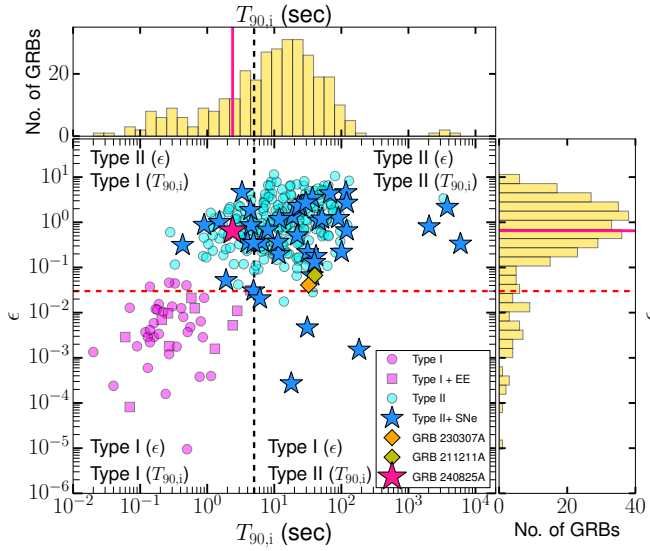


Figure 14. Rest-frame duration $T_{90,i}$ vs. ϵ for GRB 240825A (pink star), compared with the population of GRBs classified using the ϵ method (H.-J. Lü et al. 2010). The plot shows distinct regions occupied by Type I (merger-origin) and Type II (collapsar-origin) GRBs, with special populations such as Type I with EE and Type II associated with SNe (II+SNe) indicated. GRB 240825A falls within the high- ϵ , but short-duration region, clustering with classical Type I bursts ($T_{90,i}$) and Type II GRBs (ϵ), supporting a hybrid origin. GRB 230307A (marked in orange) and GRB 211211A (marked in yellow) are overlaid, demonstrating their positions relative to the classical GRB populations. The black and red dashed lines show the $T_{90,i} = 5$ sec, and $\epsilon = 0.03$, respectively.

An important tool for understanding the physical origin of GRBs lies in the classification based on their prompt emission properties. However, the traditional scheme does not always correlate well with the underlying progenitor systems, namely collapsars (Type II) and compact object mergers (Type I). To address this, H.-J. Lü et al. (2010) introduced a new phenomenological classification method based on the parameter $\epsilon \equiv E_{\gamma, \text{iso}, 52} / E_{p, z, 2}^{5/3}$, where $E_{\gamma, \text{iso}, 52}$ is the isotropic gamma-ray energy in units of 10^{52} erg and $E_{p, z, 2}$ is the rest-frame spectral peak energy in units of 100 keV. This parameter shows a clear bimodal distribution with a division at $\epsilon \sim 0.03$, effectively distinguishing Type I and Type II GRBs. In Figure 14, we plot GRB 240825A in the $\log T_{90,i} - \log \epsilon$ plane, alongside other GRBs (obtained from P. Y. Minaev & A. S. Pozanenko 2020; H. Sun et al. 2025; J. Yang et al. 2022) classified using this scheme. GRB 240825A lies in the high- ϵ , but short-duration region, clustering with classical Type I bursts ($T_{90,i}$) and Type II GRBs (ϵ), supporting a hybrid origin (merger from $T_{90,i}$ and collapsar from ϵ). This result is consistent with its observed prompt emission properties.

4.3. Machine learning-based progenitor classification of GRB 240825A

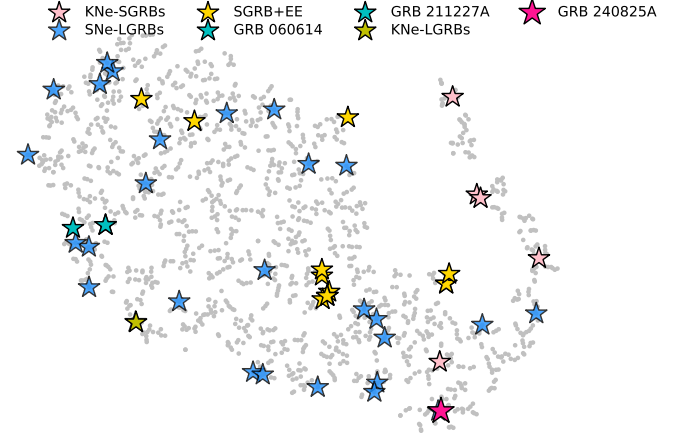


Figure 15. t-SNE classification map of *Swift* GRBs using normalized, Fourier-transformed prompt light curves as in C. K. Jespersen et al. (2020). GRB 240825A is marked with a pink star and lies near the transition between the type-L (long) and type-S (short) GRB clusters, close to the region where merger GRBs begin to dominate. The position suggests it may share characteristics with both populations, consistent with a borderline classification based on traditional T_{90} duration and spectral properties. Non-special GRBs are shown as small gray points. Light pink stars represent “Known Mergers”, blue stars denote “Known Collapsar” (e.g., GRB 190829A), and green stars, the long mergers GRB 060614 and GRB 211227A.

Recent advancements in machine learning have enabled new approaches to classify GRBs beyond traditional duration or spectral criteria. One such technique is the t-distributed stochastic neighbor embedding (t-SNE), which performs unsupervised dimensionality reduction on the high-dimensional prompt emission light curves to reveal intrinsic clustering in a lower-dimensional space (C. K. Jespersen et al. 2020). This method, applied to the full *Swift* GRB catalog, results in an unambiguous separation into two well-defined groups that broadly correspond to collapsar and merger GRBs, respectively. The t-SNE visualization reveals clustering patterns that align with physical expectations: merger GRBs occupy a region distinct from SN-associated collapsar GRBs, reflecting differences in progenitor systems. The classification is purely empirical and based on the global similarity of light curves, retaining rich temporal and spectral structure. Figure 15 presents the position of GRB 240825A on the t-SNE map along with a sample of *Swift*-detected GRBs. The burst lies just before the tail, where type-S (short) GRBs begin. Its proximity to the boundary indicates that GRB 240825A

may have prompt emission properties broadly similar to merger GRBs, though it retains some features common to collapsar bursts. Such borderline cases underscore the power of t-SNE in identifying GRBs with ambiguous classifications and point toward a continuum rather than a strict dichotomy in the prompt-emission properties of GRBs. Non-special GRBs are shown as small gray points and distinct reference sets are highlighted: Type I + KNe (light pink stars), Type I + EE (yellow stars), Type II + SNe (blue stars), comprising bursts such as GRB 230307A and GRB 211211A, known or suspected to originate from compact binary mergers, and “SN-LGRBs” (orange stars), including GRB 190829A, associated with SN signatures.

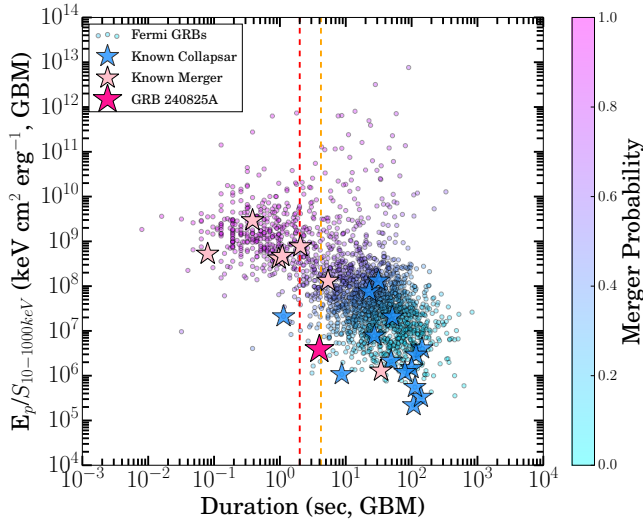


Figure 16. ML-classification of GRB 240825A (shown with pink star) in the plane of burst duration (T_{90}) versus spectral peak energy over fluence (E_p/S), following the SVM-based method of P. Nuessle et al. (2024). The color scale represents the predicted merger probability, ranging from 1 (merger-like) to 0 (collapsar-like). Known collapsars (blue stars) and known mergers (pink stars) are also shown for reference. GRB 240825A falls in a region with intermediate T_{90} and moderate E_p/S , with a classifier prediction of $\sim 76\%$ probability for a collapsar origin. The vertical orange and red lines show a 4.2 sec duration boundary from the fourth Fermi Catalog (A. von Kienlin et al. 2020) and $T_{90} = 2$ sec, respectively.

Furthermore, P. Nuessle et al. (2024) demonstrated that machine learning methods can classify GRB progenitors using prompt emission observables, moving beyond simplistic duration-based schemes. In particular, the ratio of the spectral peak energy (E_p) to fluence (S) in the 10–1000 keV band, plotted against the burst duration (T_{90}), serves as a physically motivated proxy to distinguish progenitor types, as collapsars and compact

object mergers tend to populate different regions in this plane. This methodology was adopted in a probabilistic framework using a support vector machine (SVM) with a radial basis function kernel, trained on a sample of GRBs with known progenitor associations. We applied this classifier to GRB 240825A and obtained a probability of $\sim 76\%$ for a collapsar origin and $\sim 24\%$ for a merger origin. The fourth Fermi Catalog suggested a boundary of 4.2 seconds for classifying GRBs (A. von Kienlin et al. 2020). We noted that GRB 240825A has a duration slightly below this *Fermi*-GBM threshold. Following the classification scheme proposed by P. Nuessle et al. (2024), GRB 240825A would likely be considered a short collapsar similar to GRB 200826A (see Figure 16, T. Ahumada et al. 2021). This result highlights the usefulness of SVM-based classifiers that go beyond duration-based thresholds by incorporating prompt emission spectral information.

4.4. Search for associated Supernova with GRB 240825A

Nearby long-duration GRBs are frequently connected to the core-collapse of massive stars into type Ic-BL SNe, characterized by the absence of hydrogen and helium in their spectra (S. E. Woosley & J. S. Bloom 2006). GRB 240825A exhibits a duration of approximately 4 seconds and lies at a redshift of $z = 0.659$, placing it relatively nearby in the cosmological context. The burst released a substantial fluence of $\sim 10^{-4}$ erg cm $^{-2}$, indicative of a highly energetic event and consistent with the Amati relation of collapsar GRBs. Furthermore, its X-ray afterglow luminosity is also consistent with those observed in collapsar GRBs, and significantly more luminous than typical Type I GRBs of merger origin (R. Ruffini et al. 2024). These observational signatures support the classification of GRB 240825A as a likely collapsar event, likely arising from a massive stellar collapse. Its properties are broadly consistent with the binary-driven hypernova (BdHN I) scenario (e.g., C. L. Bianco et al. 2024), indicating a core-collapse progenitor and an associated SN (R. Ruffini et al. 2024). These properties of GRB 240825A motivated us to search for an accompanying SN signature. We conducted a comprehensive search for a SN associated with the long-duration burst GRB 240825A, located at a redshift of $z = 0.659$, using optical (using the LBC mounted on the Large Binocular Telescope E. Giallongo et al. 2008), UV (*Swift*-UVOT), and near-infrared (using EMIR mounted on the 10.4m GTC Telescope) observations. Optical observations were performed in the Sloan r' and z' bands across three epochs: 2024-09-12 (~ 17.59 days post-burst), 2024-09-28 (~ 33.70 days post-burst), and 2024-11-09

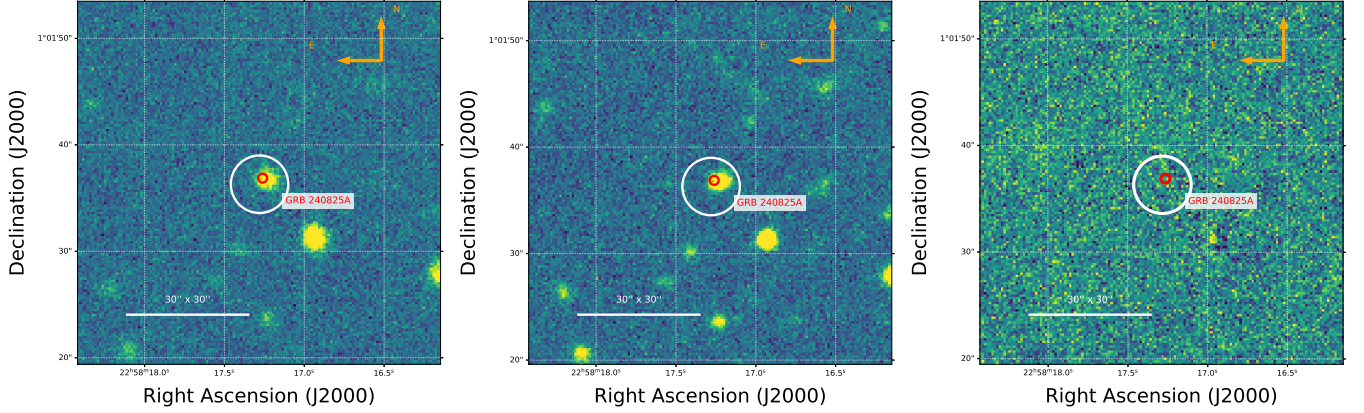


Figure 17. Lack of bright SN associated with GRB 240825A. *Left:* LBT r' -band image of the GRB 240825A field on 2024 Sept 28 (~ 33.70 days post-burst). *Middle:* LBT r' -band on 2024 Nov 9 (~ 75.52 days) used as the subtraction template. *Right:* Difference image (Sept 28 – Nov 9) produced with AutoPhot/HOTPANTS, showing no point-like residual at the GRB afterglow position (red circle). The white and red circles show the uncertainty in the position measured by *Swift*-XRT and *Swift*-UVOT. Images are oriented with north up and east to the left. The scale bar corresponds to $10''$.

(~ 75.52 days post-burst). With a time dilation factor of $1 + z = 1.659$ due to the redshift, these epochs correspond to rest-frame times of approximately 10.60, 20.31, and 45.52 days, respectively, aligning with the typical rise and decay phases of SN-GRB light curves (Z. Cano et al. 2017a). Furthermore, *Swift*-UVOT performed a deep late-time search for SN emission in the U-band up to ~ 33.14 days post-burst (see Table A4). We also utilized GTC NIR observations in the J , H , and K bands, with exposure times of 910–1260 seconds, spanned ~ 19.31 –27.41 days post-trigger (~ 11.6 –16.5 days rest frame), a period optimal for detecting SN emission near its peak (Z. Cano et al. 2017b). The choice of r' , z' , J , H , and K bands leverages their red and near-infrared coverage, ideal for detecting redshifted optical emission from a distant source at $z = 0.659$, where rest-frame ultraviolet and blue light are shifted into these wavelengths.

To identify a potential SN signature superimposed on the host galaxy’s light, we employed image subtraction using the AutoPhot software package (S. J. Brennan & M. Fraser 2022), which implements the HOTPANTS algorithm for optimal difference imaging (A. Becker 2015). This technique aligns a science image (containing the potential transient) with a template image (where the transient has faded), scales them to match in flux, and subtracts the template to remove static sources like the host galaxy. For GRB 240825A, the third epoch (2024-11-09, 75.52 days post-burst) served as the template, as any SN would have significantly faded by this late time (45.52 days rest frame), leaving primarily the host galaxy emission. This template was subtracted from the first (2024-09-12) and second (2024-09-28) epoch LBT images in both r' and z' bands. The resulting difference

images revealed no significant residual flux at the precise position of GRB 240825A, indicating the absence of a detectable SN component. For the GTC NIR data, the second epoch (~ 27.41 days) was subtracted from the first epoch (~ 19.31 days) in J , and K bands. No significant residual flux was detected in any difference images at the GRB position (derived from XRT and UVOT uncertainty circles), further indicating the absence of an SN signature. Given the non-detection of a transient source, we calculated upper limits on the brightness of any potential SN. These limits represent the faintest magnitudes detectable at a 3σ confidence level above the background noise in the difference images. For the LBT optical data, the limits are: on 2024-09-12, $r' > 26.1$ mag, $z' > 24.9$ mag; on 2024-09-28, $r' > 24.6$ mag, $z' > 23.9$ mag; and on 2024-11-09, $r' > 25.9$ mag, $z' > 25.0$ mag (AB system). For the GTC NIR data, limits at the first epoch (~ 19.31 –27.41 days) are $J > 23.4$ mag, $H > 23.3$ mag, and $K > 23.1$ mag (AB system). These values reflect the sensitivity of the observations, with variations likely due to differences in seeing conditions, exposure times, or sky brightness across epochs. Furthermore, using the UVOT data, we attempted a deep late-time search for emission from a SN potentially associated with the GRB; however, no evidence of any SN was detected up to 23.4 mag (AB) in the U-band. We limit our search to the U band, since it is the most sensitive of UVOT’s filters, and as this GRB has the most late-time coverage in the U filter. We summed the last 3 observations (during which the GRB’s emission would be the faintest; i.e., targetIDs 01250617012, 01250617013, 01250617015) using *uvotimsum* and then calculated the upper limits using *uvotsource*. To obtain even deeper

limits, we then continued to sequentially add the prior segment's U-band exposure. We repeated this until we summed the U-band exposures from targetIDs 01250617004, 01250617006, 01250617007, 01250617008, 01250617012, 01250617013, and 01250617015. The limits for the different combinations of summed images are given in Table A4.

To interpret these non-detections, we compared our upper limits to the light curves of well-characterized SN-GRBs: SN1998bw (associated with GRB 980425, T. J. Galama et al. 1998), SN2006aj (GRB 060218, S. Campana et al. 2006), SN2010bh (GRB 100316D, R. L. C. Starling et al. 2011), and SN2017iuk (GRB 171205A, L. Izzo et al. 2019) and KN-GRB: AT2017gfo (V. A. Villar et al. 2017). These light curves were adjusted to the redshift of GRB 240825A ($z = 0.659$) by applying a time dilation factor of 1.659 to stretch the temporal axis and a distance modulus correction to account for luminosity distance differences. Additionally, we compared our NIR limits to a sample of GRB-SNe with detected NIR emission (G. Finneran et al. 2025), as shown in the NIR light curve comparison (see Figure 18). Our optical and NIR limits are significantly deeper than the expected magnitudes of the brightest SNe at comparable rest-frame epochs (see light curve comparison in Figure 18). For example, SN1998bw, one of the brightest known SN-GRBs, would appear significantly brighter (e.g., ~ 23.7 mag in r' at peak) than our deepest limits if placed at $z = 0.659$, and thus would have been readily detected. The non-detection across all epochs therefore excludes the presence of an SN as luminous as these archetypes, implying that any SN associated with GRB 240825A must be substantially fainter or absent entirely. The non-detection across optical and NIR bands also suggests either a low-luminosity SN component below our detection limits or a GRB without a detectable SN, potentially indicating diverse physical mechanisms or progenitor properties (A. M. Soderberg et al. 2010). These deep limits, particularly in the NIR, where dust extinction is less significant, strengthen the constraint against a bright SN. On the other hand, emission from AT2017gfo-like KN (V. A. Villar et al. 2017) at $z = 0.659$ is significantly fainter than our limits.

For the non-detection of an SN associated with GRB 240825A, observed using the LBT with an r -band magnitude limit of $m_r > 26.1$ at approximately 17.59 days post-burst (observer frame), we derived an extinction-corrected absolute magnitude upper limit of $M_r > -17.58$ mag (with k -correction). Applying a bolometric correction of -0.43 to account for flux outside the observed band (S. J. Prentice et al. 2016), we obtained a bolometric absolute magnitude limit of $M_{\text{bol}} > -18.01$

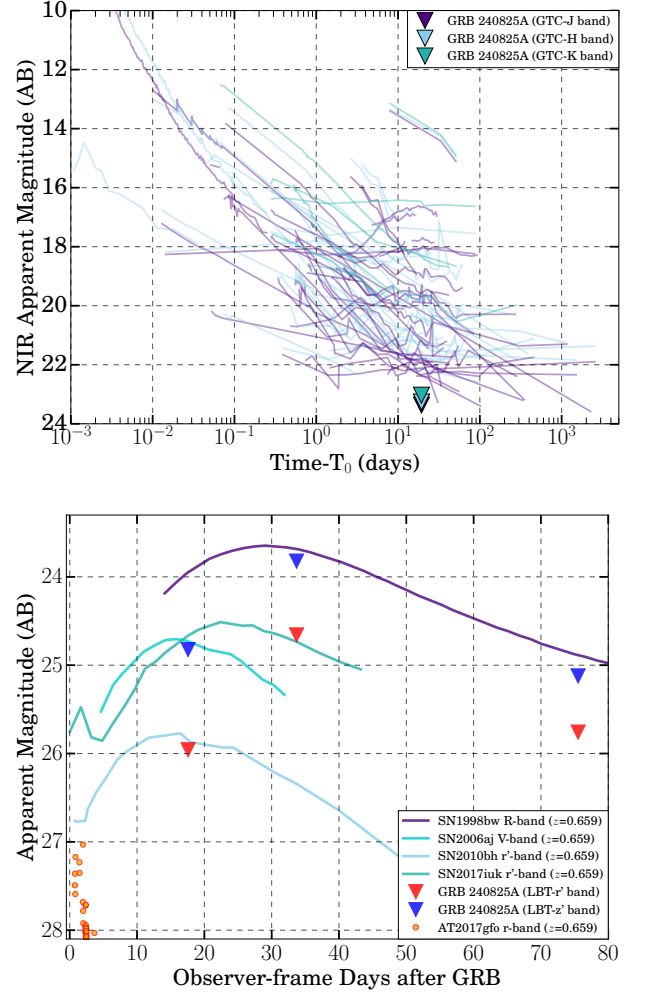


Figure 18. Comparison of our deep optical-NIR limits for GRB 240825A with well-studied GRB-associated SNe. (a) NIR light curves in the J (indigo), H (sky blue), and K (light sea green) bands from GTC observations of GRB 240825A, along with the NIR light curves for a GRB-SN sample obtained from G. Finneran et al. (2025). (b) Optical deep limits in the r and z bands from LBT observations of GRB 240825A, compared to SN1998bw, SN2006aj, SN2010bh, and SN2017iuk (G. Finneran et al. 2025) and KN AT2017gfo (V. A. Villar et al. 2017) scaled to the redshift of GRB 240825A ($z = 0.659$).

(with k -correction), corresponding to a bolometric luminosity upper limit of $L_{\text{bol}} < 4.82 \times 10^{42}$ erg/sec. Assuming that any accompanying SN would be powered by the radioactive decay chain $^{56}\text{Ni} \rightarrow ^{56}\text{Co} \rightarrow ^{56}\text{Fe}$ (e.g., W. D. Arnett 1982; S. Valenti et al. 2008; Y. D. Hu et al. 2021), we used the standard heating function, which relates the bolometric luminosity to the nickel mass via $L_{\text{bol}}(t) = \frac{M_{\text{Ni}}}{M_{\odot}} \cdot [(\epsilon_{\text{Ni}} - \epsilon_{\text{Co}})e^{-t/t_{\text{Ni}}} + \epsilon_{\text{Co}}e^{-t/t_{\text{Co}}}]$ (D. Branch & J. C. Wheeler 2017), where t is the rest-frame time since explosion. Converting the observer

frame time to rest frame using $t_{\text{rest}} = t_{\text{obs}}/(1+z) = 17.59/1.659 \approx 10.60$ days, and using standard values $\varepsilon_{\text{Ni}} = 7.9 \times 10^{43}$ erg/sec, $\varepsilon_{\text{Co}} = 1.45 \times 10^{43}$ erg/sec, $t_{\text{Ni}} = 8.8$ days, and $t_{\text{Co}} = 111.3$ days (Z. Bora et al. 2022), we estimate an upper limit on the synthesized nickel mass of $M_{\text{Ni}} \lesssim 0.15 M_{\odot}$. This limit is lower than the typical ^{56}Ni masses observed in GRB-associated SN, which have a medium value approximately 0.3 to 0.35 M_{\odot} (Z. Cano 2013). For comparison, SN 1998bw had an $M_{\text{Ni}} \approx 0.4 M_{\odot}$ (K. Iwamoto et al. 1998) and SN 2003dh had an $M_{\text{Ni}} \approx 0.35 M_{\odot}$ (P. A. Mazzali et al. 2003). As the amount of the nickel synthesized determines the peak of an SN powered by the radioactive decay chain $^{56}\text{Ni} \rightarrow ^{56}\text{Co} \rightarrow ^{56}\text{Fe}$, the low inferred M_{Ni} suggests that any accompanying SN to GRB 240825A must be unusually faint, otherwise the progenitor scenario may differ from classical collapsar events.

To search for a potential SN associated with GRB 240825A, we obtained late-time photometry in the observer-frame z -band, which probes the rest-frame V -band at the burst redshift ($z = 0.659$). Based on our non-detections, we derive upper limits on the absolute magnitude. For a rest-frame SN peak time of 10.6 days (observer-frame 17.58 days), the limit is $M_V > -18.16$, while for a later peak at 20.3 days (observer-frame 33.70 days), we obtain $M_V > -19.16$. We placed these values of GRB 240825A in the distribution of peak absolute V -band magnitude (M_V) versus rest-frame peak time (T_{max}) for GRB-associated SN. These constraints are shown in Figure 19, alongside the GRB-SN sample from S. O. Belkin & A. S. Pozanenko (2024). GRB 240825A falls below the median peak brightness range of the GRB-SNe population, suggesting that any associated SN is either intrinsically faint, rapidly evolving, or entirely absent. This result underscores the observational diversity among GRB-SNe and may hint at alternative progenitor scenarios beyond the canonical collapsar model.

We explored the possible cause (such as the local environment) of the non-detection of the associated SN for GRB 240825A. GRBs offer a unique probe into the interstellar medium and star-forming environments of their host galaxies. The visual extinction (A_V), defined as the attenuation of light in the visual band due to dust along the line of sight, serves as a critical indicator of the dust content and density of the ISM. Based on the afterglow analysis using UVOT and XRT data, we derive a color excess of ($E(B-V) = 0.31$) and a visual extinction of ($A_V = 0.99$) for LMC, indicating significant dust attenuation along the line of sight of GRB 240825A. In addition, we modeled the host galaxy’s stellar population using *Prospector*, which yielded an indepen-

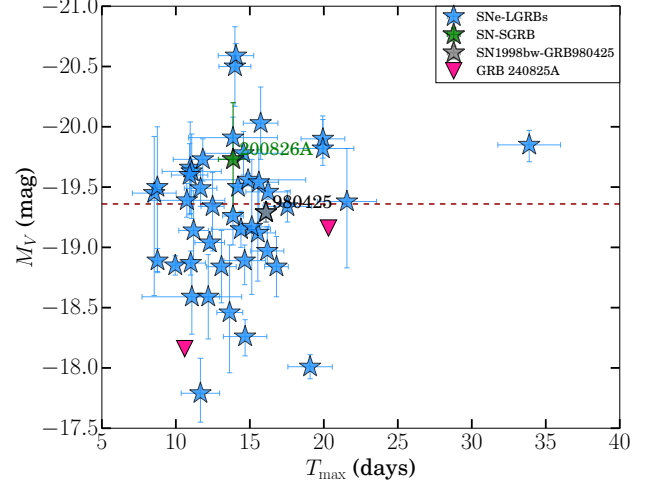


Figure 19. Distribution of peak absolute V -band magnitude (M_V) versus rest-frame peak time (T_{max}) for GRB-associated SN. Blue stars represent SNe-LGRBs, green stars denote SN-SGRB (GRB 200826A), and the grey star marks SN 1998bw associated with GRB 980425. The pink triangles indicate upper limits for GRB 240825A, derived from our z -band observations, which correspond to the rest-frame V -band at $z = 0.659$. We assume two possible peak times: $T_{\text{max}} = 17.58/(1+z) \approx 10.6$ days and $T_{\text{max}} = 33.70/(1+z) \approx 20.3$ days, corresponding to magnitude limits of $M_V > -18.16$ and $M_V > -19.16$, respectively. Data points for comparison are taken from S. O. Belkin & A. S. Pozanenko (2024), and the brown dashed line marks the median peak brightness of the SN-LGRB population.

dent estimate of the galaxy-integrated dust attenuation. From the host SED fitting, we found a best-fit value of $A_V^{\text{host}} \approx 1.73$, further supporting the presence of substantial dust within the host galaxy. In this study, we investigate the A_V as a function of redshift (z) for GRB 240825A, comparing it with a well-established sample of GRBs from prior works (D. A. Kann et al. 2006, 2010; T. Krühler et al. 2011; P. Schady et al. 2012). This combination of high LOS extinction and significant host-integrated attenuation places GRB 240825A among the more dust-obscured events at its redshift relative to the broader GRB population, suggesting an unusually dust-rich host galaxy (see Figure 20). This high extinction implies a dense ISM, potentially rich in star-forming material, which may influence the observed properties of the GRB and associated phenomena, such as SNe. Notably, despite extensive follow-up observations in the NIR, UV, and optical bands, no SN counterpart was detected for GRB 240825A, which could be attributed to this substantial dust obscuration. Across the GRB sample, we observe a general trend of decreasing A_V with increasing redshift, likely driven by selection bi-

ases inherent in high-redshift observations (D. A. Kann et al. 2010; R. Gupta et al. 2022a). At higher redshifts ($z \geq 5$), the detection of dusty galaxies (A. J. Castro-Tirado et al. 2024) becomes increasingly difficult due to cosmological dimming, the redshift of rest-frame ultraviolet light into the optical and NIR regimes (where dust extinction effects are less severe), and the limited sensitivity of current telescopes to faint, obscured sources.

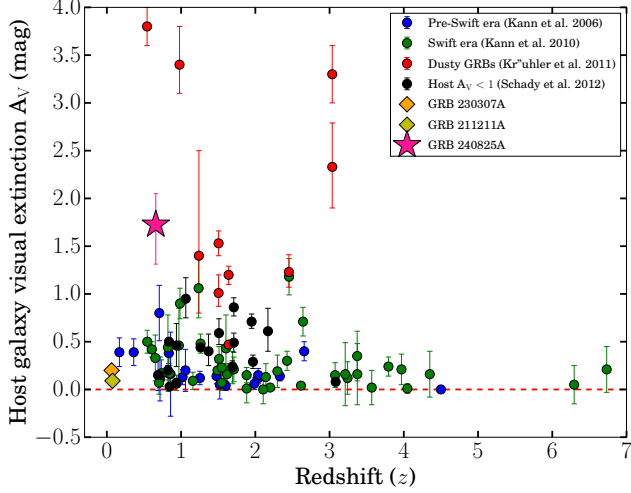


Figure 20. The figure illustrates the relationship between host galaxy visual extinction (A_V) and redshift (z) for GRB 240825A alongside various GRB samples, with the horizontal red dashed line indicating $A_V = 0$. Our analysis reveals that GRB 240825A exhibits a significantly elevated A_V at its redshift relative to the broader GRB population.

5. CONCLUSION

In this study, we have performed a detailed, multi-wavelength investigation of GRB 240825A—a unique gamma-ray burst that challenges the traditional dichotomy between short and long GRBs. With a prompt duration of ~ 4 s and an ambiguous placement in the T_{90} –hardness parameter space, GRB 240825A exemplifies the growing population of hybrid events that defy simple classification. Classical diagnostics such as the minimum variability timescale, spectral lag, and low sSFR suggest similarities with Type I GRBs originating from compact binary mergers. However, its high fluence, EE tail, and placement within the $E_{p,i}$ – $E_{\gamma,iso}$ (Amati) relation favor an interpretation more consistent with collapsar-driven long GRBs. These findings underscore the limitations of duration-based classification alone and necessitate a more comprehensive approach.

To further refine its classification, we employed advanced machine-learning classifiers (e.g., t-SNE, support vector machines) and modern physical metrics such

as the energy-hardness-duration parameter, and $\varepsilon = E_{\gamma,iso,52}/E_{p,z,2}^{5/3}$. These approaches consistently indicate that GRB 240825A exhibits mixed properties (e.g., SVM suggest a probability of $\sim 76\%$ for a collapsar origin and $\sim 24\%$ for a merger origin). Timing analysis of GRB 240825A, conducted using light curves from the ASIM-HED and *Fermi*-GBM, reveals low-significance peaks at approximately 6 Hz and 20 Hz in the Power Density Spectra. These weak QPOs suggest possible variability in the central engine or jet dynamics, but their low significance precludes definitive conclusions about the progenitor. Although the QPOs exhibit statistically low significance, the consistent appearance of analogous features at approximately the same frequency in both the *Fermi* and ASIM datasets suggests that the phenomenon may have a physical basis, despite the lack of robust confirmation.

Late-time photometric and spectroscopic follow-up with the 10.4 m GTC, LBT, and *Swift*/UVOT revealed no detectable SN or KN component down to deep limits ($m_r > 26.1$, $m_J > 23.4$, $m_H > 23.3$, and $m_K > 23.1$ AB mag), despite relatively nearby redshift of $z = 0.659$. The absence of bright SN features, especially those similar to SN 1998bw, raises two possibilities: either the SN was intrinsically faint (low luminosity SN with absolute magnitude M_V fainter than -18.0 mag), or it was heavily extinguished by dust in the host environment. We estimate an upper limit on the synthesized nickel mass of $M_{Ni} \lesssim 0.15 M_{\odot}$. This limit is lower than the typical ^{56}Ni masses observed in GRB-associated SN.

Indeed, SED modeling of the host galaxy with *Prospector* reveals a massive, dusty, and actively star-forming system, typical of collapsar GRB environments. The physical offset of GRB 240825A from the host centroid (~ 4.54 kpc), derived from the host position and VLA position, lies intermediate between distributions typically seen in collapsar and merger GRBs. This spatial context, coupled with the deep non-detections of associated SN, may imply a highly obscured SN or an atypical progenitor channel.

In summary, GRB 240825A is an archetypal example of a GRB that lies near the boundary of current classification schemes. Its short-timescale variability, ambiguous prompt diagnostics, lack of a bright SN signature, and host galaxy context highlight the limitations of duration-based classification. This burst reinforces the need for a unified framework that combines prompt emission physics, afterglow behavior, host galaxy properties, and contextual progenitor signatures. Future studies, particularly those leveraging high-cadence multiwavelength follow-up and statistical learning techniques, will be essential to identify and interpret such

hybrid events within the broader landscape of GRB phenomenology.

ACKNOWLEDGMENTS

RG was sponsored by the National Aeronautics and Space Administration (NASA) through a contract with ORAU. The views and conclusions contained in this document are those of the authors and should not be interpreted as representing the official policies, either expressed or implied, of the National Aeronautics and Space Administration (NASA) or the U.S. Government. The U.S. Government is authorized to reproduce and distribute reprints for Government purposes notwithstanding any copyright notation herein. AR acknowledges support by PRIN-MIUR 2017 (grant 20179ZF5KS). AJCT acknowledges support from the Spanish Ministry project PID2023-151905OB-I00 and Junta de Andalucía grant P20_010168 and from the Severo Ochoa grant CEX2021-001131-S funded by MCIN/AEI/10.13039/501100011033. Based on observations collected at the Observatorio de Sierra Nevada (operated by IAA-CSIC) and at the Centro Astronómico Hispano en Andalucía (CAHA) at Calar Alto (proposal 24B-2.2-010), operated jointly by Junta de Andalucía and Consejo Superior de Investigaciones Científicas (IAA-CSIC). Also based on observations made with the Gran Telescopio Canarias (GTC) (proposal GTCMULTIPLE7B-24B 104-MULTIPLE-7/24A), installed at the Spanish Observatorio del Roque de los Muchachos of the Instituto de Astrofísica de Canarias, on the island of La Palma. This work is partly based on data obtained with the instrument OSIRIS, built by a Consortium led by the Instituto de Astrofísica de Canarias in collaboration with the

Instituto de Astronomía of the Universidad Autónoma de México. OSIRIS was funded by GRANTECAN and the National Plan of Astronomy and Astrophysics of the Spanish Government. MCG acknowledges support from the Spanish Ministry project PID2023-149817OB-C31. The programme of development within Priority-2030 is acknowledged for supporting the research at UrFU. ASIM is a mission of ESA’s SciSpace programme for scientific utilization of the *ISS* and non-*ISS* space exploration platforms and space environment analogues. ASIM and the ASIM Science Data Centre are funded by ESA and by national grants of Denmark, Norway and Spain. This research has used data obtained through the HEASARC Online Service, provided by the NASA-GSFC, in support of NASA High Energy Astrophysics Programs. This work made use of data supplied by the UK Swift Science Data Centre at the University of Leicester. The LBT is an international collaboration of the University of Arizona, Italy (INAF: Istituto Nazionale di Astrofisica), Germany (LBTB: LBT Beteiligungsgesellschaft), The Ohio State University, representing also the University of Minnesota, the University of Virginia, and the University of Notre Dame. LH acknowledges support from Research Ireland grant 19/FFP/6777. DT acknowledges support from the National Research Foundation of Korea (NRF) grant, No.2020R1A2C3011091, and No.2021M3F7A1084525, and RS-2024-00343729, funded by the Korea government (MSIT).

Facilities: Swift(BAT, XRT, and UVOT), Fermi, ASIM, GTC, LBT, OSN, BOOTES, CAHA, IKI-FuN

Software: astropy (Astropy Collaboration et al. 2013, 2018, 2022), XSPEC (K. A. Arnaud 1996), Source Extractor (E. Bertin & S. Arnouts 1996)

APPENDIX

A. FIGURE AND TABLE

REFERENCES

- Abbott, B. P., Abbott, R., Abbott, T. D., et al. 2017a, *ApJL*, 848, L12, doi: [10.3847/2041-8213/aa91c9](https://doi.org/10.3847/2041-8213/aa91c9)
- Abbott, B. P., Abbott, R., Abbott, T. D., et al. 2017b, *PhRvL*, 119, 161101, doi: [10.1103/PhysRevLett.119.161101](https://doi.org/10.1103/PhysRevLett.119.161101)
- Ahumada, T., Singer, L. P., Anand, S., et al. 2021, *Nature Astronomy*, 5, 917, doi: [10.1038/s41550-021-01428-7](https://doi.org/10.1038/s41550-021-01428-7)
- Amati, L., Frontera, F., Tavani, M., et al. 2002, *A&A*, 390, 81, doi: [10.1051/0004-6361:20020722](https://doi.org/10.1051/0004-6361:20020722)
- Arnaud, K. A. 1996, in *Astronomical Society of the Pacific Conference Series*, Vol. 101, *Astronomical Data Analysis Software and Systems V*, ed. G. H. Jacoby & J. Barnes, 17
- Arnett, W. D. 1982, *ApJ*, 253, 785, doi: [10.1086/159681](https://doi.org/10.1086/159681)

Table A1. *Swift*-UVOT observations of GRB 240825A. The table lists the mid-time of observations (T–T0), half exposure time, AB magnitude with errors, and upper limits (3σ) for cases with S/N < 2. All measurements are in the AB magnitude system.

Telescope	Filter	T–T0 (sec)	Exp. (sec)	AB Mag \pm Error
Swift-UVOT	WH	102.99740	10.00000	15.612 \pm 0.036
Swift-UVOT	WH	122.99740	10.00000	15.871 \pm 0.037
Swift-UVOT	WH	142.99740	10.00000	16.253 \pm 0.041
Swift-UVOT	WH	167.99740	15.00000	16.470 \pm 0.035
Swift-UVOT	WH	202.99740	20.00000	16.781 \pm 0.034
Swift-UVOT	WH	232.87380	9.87640	16.976 \pm 0.052
Swift-UVOT	WH	594.91400	9.88150	18.365 \pm 0.104
Swift-UVOT	WH	767.51850	9.87600	18.574 \pm 0.118
Swift-UVOT	WH	1170.87090	9.87590	19.161 \pm 0.206
Swift-UVOT	WH	6095.52310	99.89210	20.586 \pm 0.165
Swift-UVOT	V	77.82920	5.00000	13.625 \pm 0.068
Swift-UVOT	V	644.85540	9.87690	16.997 \pm 0.261
Swift-UVOT	V	817.11690	9.88140	17.025 \pm 0.266
Swift-UVOT	V	1134.47400	96.11000	17.661 \pm 0.298
Swift-UVOT	V	5069.72090	99.88650	19.098 \pm 0.424
Swift-UVOT	V	10883.36850	453.36470	20.196 \pm 0.538
Swift-UVOT	V	53432.26540	3390.49850	< 20.059 (3σ)
Swift-UVOT	V	81813.87990	3405.69650	< 20.121 (3σ)
Swift-UVOT	B	570.52030	9.88160	17.393 \pm 0.185
Swift-UVOT	B	743.22400	9.87600	17.650 \pm 0.220
Swift-UVOT	B	1146.45580	9.87660	18.845 \pm 0.795
Swift-UVOT	B	5890.87900	99.88650	20.240 \pm 0.616
Swift-UVOT	U	335.41420	30.00000	17.767 \pm 0.087
Swift-UVOT	U	405.41420	40.00000	18.035 \pm 0.087
Swift-UVOT	U	490.41420	45.00000	18.057 \pm 0.083
Swift-UVOT	U	545.29720	9.88300	18.240 \pm 0.210
Swift-UVOT	U	718.32840	9.88170	18.990 \pm 0.357
Swift-UVOT	U	1204.12500	92.42510	19.120 \pm 0.382
Swift-UVOT	U	5685.01030	99.89210	20.318 \pm 0.279
Swift-UVOT	U	40602.84590	329.04030	< 21.426 (3σ)
Swift-UVOT	U	143988.61540	8738.43570	< 22.226 (3σ)
Swift-UVOT	U	178393.99880	9192.96970	< 22.249 (3σ)
Swift-UVOT	U	246282.46700	20264.49860	< 22.406 (3σ)
Swift-UVOT	U	377364.80130	37202.24030	< 23.069 (3σ)
Swift-UVOT	U	425514.30050	692.72390	22.834 \pm 1.586
Swift-UVOT	UVW1	5480.11240	99.88650	20.929 \pm 0.383
Swift-UVOT	UVW1	34758.21760	408.60420	< 22.214 (3σ)
Swift-UVOT	UVM2	5274.65740	99.88650	21.945 \pm 0.884
Swift-UVOT	UVM2	11449.02620	107.17380	22.714 \pm 3.395
Swift-UVOT	UVW2	4865.04370	99.88100	< 21.426 (3σ)
Swift-UVOT	UVW2	6301.23740	99.88650	22.303 \pm 1.101
Swift-UVOT	UVW2	44520.64640	266.27400	23.028 \pm 1.960
Swift-UVOT	UVW2	86962.40790	2930.34870	< 23.389 (3σ)

Table A2. Optical afterglow observations of GRB 240825A with the 1.5m OSN and the 0.6m BOOTES-6/DPRT.

Telescope	Filter	T–T0 (sec)	Exp. (sec)	AB Mag \pm Error
OSN	<i>B</i>	30176	300	21.43 ± 0.17
OSN	<i>B</i>	31419	300	21.46 ± 0.17
OSN	<i>B</i>	32663	300	21.70 ± 0.19
OSN	<i>B</i>	33904	300	21.68 ± 0.22
OSN	<i>B</i>	35769	600	21.72 ± 0.14
OSN	<i>B</i>	38871	900	22.20 ± 0.24
OSN	<i>V</i>	30486	300	20.54 ± 0.15
OSN	<i>V</i>	31762	300	20.41 ± 0.12
OSN	<i>V</i>	32970	300	20.44 ± 0.12
OSN	<i>V</i>	34210	300	20.87 ± 0.18
OSN	<i>V</i>	35455	300	21.25 ± 0.24
OSN	<i>V</i>	37944	900	21.32 ± 0.09
OSN	<i>I</i>	31103	300	19.83 ± 0.07
OSN	<i>I</i>	32348	300	19.93 ± 0.08
OSN	<i>I</i>	33589	300	19.98 ± 0.08
OSN	<i>I</i>	34830	300	19.94 ± 0.08
OSN	<i>I</i>	36077	300	19.99 ± 0.07
OSN	<i>I</i>	37320	300	19.98 ± 0.07
OSN	<i>I</i>	38560	300	19.94 ± 0.08
OSN	<i>I</i>	39801	300	20.00 ± 0.08
OSN	<i>I</i>	41041	300	20.06 ± 0.09
OSN	<i>R</i>	30796	300	20.22 ± 0.11
OSN	<i>R</i>	32037	300	20.48 ± 0.10
OSN	<i>R</i>	33282	300	20.33 ± 0.10
OSN	<i>R</i>	34521	300	20.38 ± 0.09
OSN	<i>R</i>	35767	300	20.46 ± 0.10
OSN	<i>R</i>	37013	300	20.37 ± 0.09
OSN	<i>R</i>	38250	300	20.47 ± 0.12
OSN	<i>R</i>	39493	300	20.52 ± 0.12
OSN	<i>R</i>	40730	300	20.47 ± 0.10
BOOTES-6	<i>R</i>	9063	600	19.30 ± 0.18
BOOTES-6	<i>R</i>	10871	1200	19.44 ± 0.18
BOOTES-6	<i>R</i>	13159	1200	19.32 ± 0.10
BOOTES-6	<i>R</i>	15386	1200	19.60 ± 0.10
BOOTES-6	<i>R</i>	17379	1200	20.07 ± 0.11
BOOTES-6	<i>R</i>	19853	1680	20.08 ± 0.11

NOTE—AB magnitudes are reported without corrections for Galactic or host extinction. T–T0 represents the time since the GRB trigger, and Exp. is the exposure time in seconds. BOOTES-6/DPRT *R*-band magnitudes were converted from Vega to AB magnitudes using a zero-point offset of 0.21 mag.

Table A3. Optical afterglow observations of GRB 240825A with GRB IKI-FuN up to ~ 4 days after trigger.

Telescope	Filter	T-T ₀ (sec)	Exp. (sec)	Mag \pm Error
AZT-22	<i>R</i>	7827	300	18.96 ± 0.03
AZT-22	<i>R</i>	8151	300	19.04 ± 0.03
AZT-22	<i>R</i>	8476	300	19.07 ± 0.03
AZT-22	<i>R</i>	8800	300	19.09 ± 0.03
AZT-22	<i>R</i>	9125	300	19.08 ± 0.03
AZT-22	<i>R</i>	9449	300	19.16 ± 0.03
AZT-22	<i>R</i>	108002	3000	21.46 ± 0.08
AZT-22	<i>B</i>	102975	4200	22.59 ± 0.09
AZT-22	<i>R</i>	185045	4200	21.85 ± 0.07
AZT-22	<i>R</i>	268488	5100	21.85 ± 0.07
RC-35 (Kitab)	<i>Clear</i>	17876	3600	> 18.3
Zeiss-1000 (TSHAO)	<i>R</i>	84755	3600	> 21.3
Zeiss-1000(SAO)	<i>R</i>	21078	3000	> 19.5
Zeiss-1000(SAO)	<i>R</i>	115706	3600	> 21.0
Zeiss-1000(SAO)	<i>R</i>	189626	4200	21.88 ± 0.07
Zeiss-1000(SAO)	<i>R</i>	274672	5400	22.15 ± 0.07

NOTE—The magnitudes are reported in Vega without corrections for Galactic or host extinction. T-T₀ represents the time since the GRB trigger, and Exp. is the exposure time in seconds.

Table A4. Late-time *Swift*/UVOT Observations for SN Search Associated with GRB 240825A.

Start Time (days, T-T ₀)	Stop Time (days, T-T ₀)	Exposure (sec)	Filter	Mag Limit (AB, 3σ)
24.73	33.14	6030	U	22.75
3.94	33.14	7532	U	22.87
4.73	33.14	11070	U	23.09
2.62	33.14	14487	U	23.24
1.57	33.14	18232	U	23.37
0.47	33.14	18872	U	23.39

NOTE—All observations were performed in the UVOT *U* band. Magnitudes represent 3σ upper limits and have not been corrected for Galactic extinction.

Astropy Collaboration, Robitaille, T. P., Tollerud, E. J., et al. 2013, *A&A*, 558, A33, doi: [10.1051/0004-6361/201322068](https://doi.org/10.1051/0004-6361/201322068)

Astropy Collaboration, Price-Whelan, A. M., Sipőcz, B. M., et al. 2018, *AJ*, 156, 123, doi: [10.3847/1538-3881/aabc4f](https://doi.org/10.3847/1538-3881/aabc4f)

Astropy Collaboration, Price-Whelan, A. M., Lim, P. L., et al. 2022, *ApJ*, 935, 167, doi: [10.3847/1538-4357/ac7c74](https://doi.org/10.3847/1538-4357/ac7c74)

Barthelmy, S. D., Barbier, L. M., Cummings, J. R., et al. 2005, *SSRv*, 120, 143, doi: [10.1007/s11214-005-5096-3](https://doi.org/10.1007/s11214-005-5096-3)

Becker, A. 2015,, *Astrophysics Source Code Library*, record ascl:1504.004

Belkin, S. O., & Pozanenko, A. S. 2024, *Astronomy Letters*, 50, 701, doi: [10.1134/S1063773725700069](https://doi.org/10.1134/S1063773725700069)

Berger, E. 2014a, *ARA&A*, 52, 43, doi: [10.1146/annurev-astro-081913-035926](https://doi.org/10.1146/annurev-astro-081913-035926)

Berger, E. 2014b, *ARA&A*, 52, 43, doi: [10.1146/annurev-astro-081913-035926](https://doi.org/10.1146/annurev-astro-081913-035926)

Bernardini, M. G., Ghirlanda, G., Campana, S., et al. 2015, *MNRAS*, 446, 1129, doi: [10.1093/mnras/stu2153](https://doi.org/10.1093/mnras/stu2153)

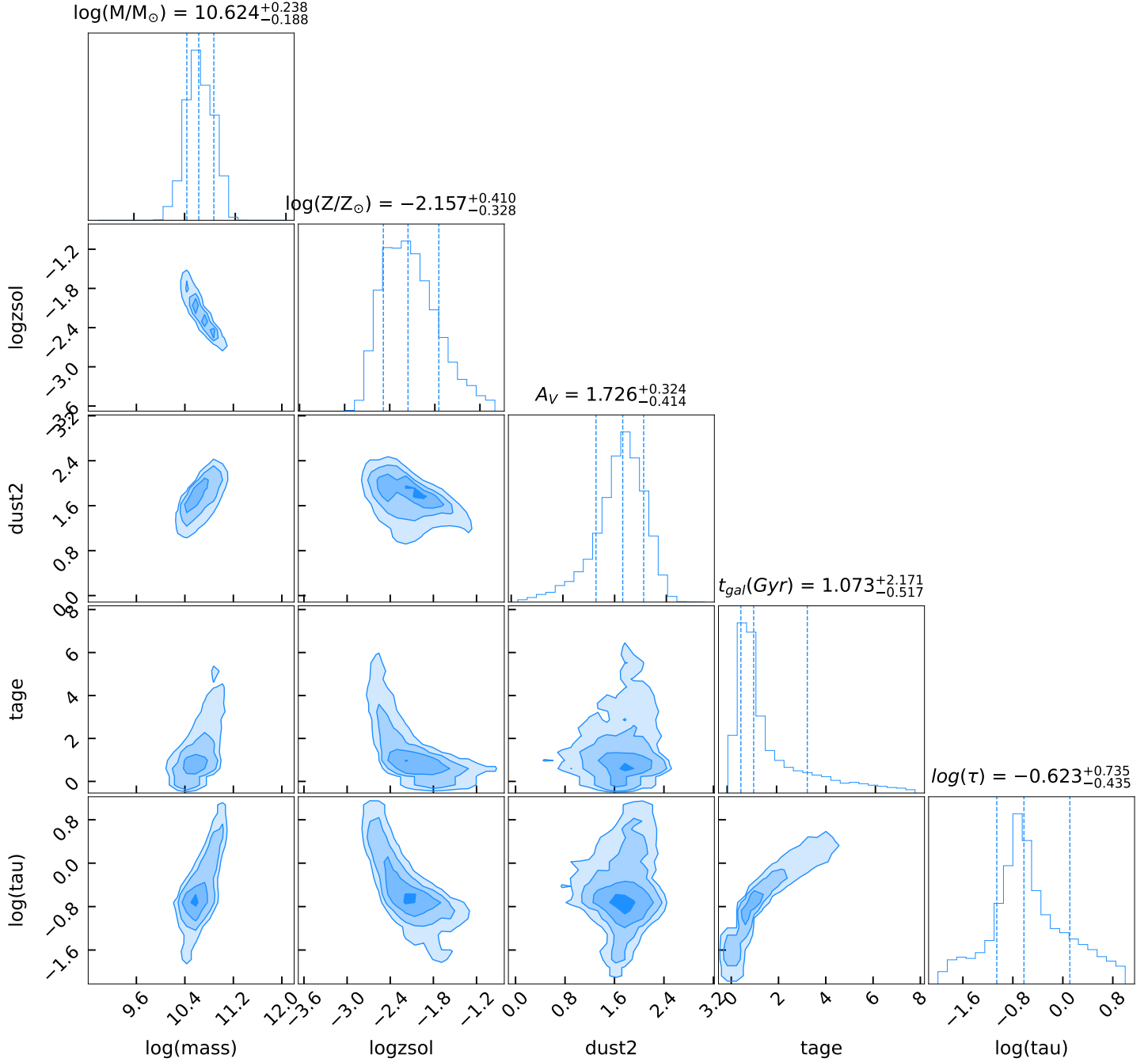


Figure A1. Corner plot illustrating the posterior distributions of host SED model parameters obtained using **Prospector**: stellar mass ($\log(M/M_\odot)$) and star formation timescale ($\log(\tau/\text{yr})$), dust, from the MCMC fitting process. The contours represent 68% and 95% confidence intervals. The best-fit values are marked with blue lines.

Bertin, E., & Arnouts, S. 1996, *A&AS*, 117, 393,
doi: [10.1051/aas:1996164](https://doi.org/10.1051/aas:1996164)

Bianco, C. L., Mirtorabi, M. T., Moradi, R., et al. 2024,
ApJ, 966, 219, doi: [10.3847/1538-4357/ad2fa9](https://doi.org/10.3847/1538-4357/ad2fa9)

Blanchard, P. K., Berger, E., & Fong, W.-f. 2016, *ApJ*, 817,
144, doi: [10.3847/0004-637X/817/2/144](https://doi.org/10.3847/0004-637X/817/2/144)

Bora, Z., Vinkó, J., & Könyves-Tóth, R. 2022, *PASP*, 134,
054201, doi: [10.1088/1538-3873/ac63e7](https://doi.org/10.1088/1538-3873/ac63e7)

Branch, D., & Wheeler, J. C. 2017, *Supernova Explosions*,
doi: [10.1007/978-3-662-55054-0](https://doi.org/10.1007/978-3-662-55054-0)

- Breeveld, A. A., Landsman, W., Holland, S. T., et al. 2011, in American Institute of Physics Conference Series, Vol. 1358, American Institute of Physics Conference Series, ed. J. E. McEnery, J. L. Racusin, & N. Gehrels, 373–376, doi: [10.1063/1.3621807](https://doi.org/10.1063/1.3621807)
- Brennan, S. J., & Fraser, M. 2022, *A&A*, 667, A62, doi: [10.1051/0004-6361/202243067](https://doi.org/10.1051/0004-6361/202243067)
- Brivio, R., Ferro, M., D’Avanzo, P., et al. 2024, GRB Coordinates Network, 37295, 1
- Bromberg, O., Nakar, E., Piran, T., & Sari, R. 2013, *ApJ*, 764, 179, doi: [10.1088/0004-637X/764/2/179](https://doi.org/10.1088/0004-637X/764/2/179)
- Burns, E., Svinkin, D., Fenimore, E., et al. 2023, *ApJL*, 946, L31, doi: [10.3847/2041-8213/acc39c](https://doi.org/10.3847/2041-8213/acc39c)
- Burrows, D. N., Hill, J. E., Nousek, J. A., et al. 2005, *SSRv*, 120, 165, doi: [10.1007/s11214-005-5097-2](https://doi.org/10.1007/s11214-005-5097-2)
- Caballero-García, M. D., Gupta, R., Pandey, S. B., et al. 2023, *MNRAS*, 519, 3201, doi: [10.1093/mnras/stac3629](https://doi.org/10.1093/mnras/stac3629)
- Caballero-García, M. D., Göğüş, E., Navarro-González, J., et al. 2025, *MNRAS*, 538, L100, doi: [10.1093/mnrasl/slaf016](https://doi.org/10.1093/mnrasl/slaf016)
- Campana, S., Mangano, V., Blustin, A. J., et al. 2006, *Nature*, 442, 1008, doi: [10.1038/nature04892](https://doi.org/10.1038/nature04892)
- Cano, Z. 2013, *MNRAS*, 434, 1098, doi: [10.1093/mnras/stt1048](https://doi.org/10.1093/mnras/stt1048)
- Cano, Z., Wang, S.-Q., Dai, Z.-G., & Wu, X.-F. 2017a, *Advances in Astronomy*, 2017, 8929054, doi: [10.1155/2017/8929054](https://doi.org/10.1155/2017/8929054)
- Cano, Z., Izzo, L., de Ugarte Postigo, A., et al. 2017b, *A&A*, 605, A107, doi: [10.1051/0004-6361/201731005](https://doi.org/10.1051/0004-6361/201731005)
- Castro-Tirado, A. J. 2023, *Nature Astronomy*, 7, 1136, doi: [10.1038/s41550-023-02075-w](https://doi.org/10.1038/s41550-023-02075-w)
- Castro-Tirado, A. J., Gupta, R., Pandey, S. B., et al. 2024, *A&A*, 683, A55, doi: [10.1051/0004-6361/202346042](https://doi.org/10.1051/0004-6361/202346042)
- Cheng, Y., Pan, Y., Yang, Y.-P., et al. 2025, *ApJ*, 979, 38, doi: [10.3847/1538-4357/ad9ea1](https://doi.org/10.3847/1538-4357/ad9ea1)
- Dallessi, S., Veres, P., Hui, C. M., et al. 2025, arXiv e-prints, arXiv:2507.12637, doi: [10.48550/arXiv.2507.12637](https://doi.org/10.48550/arXiv.2507.12637)
- Della Valle, M., Chincarini, G., Panagia, N., et al. 2006, *Nature*, 444, 1050, doi: [10.1038/nature05374](https://doi.org/10.1038/nature05374)
- Di Lalla, N., Gupta, R., Holzmann, A., & Fermi-LAT Collaboration. 2024, GRB Coordinates Network, 37288, 1
- Evans, P. A., Goad, M. R., Osborne, J. P., Beardmore, A. P., & Swift-XRT Team. 2024, GRB Coordinates Network, 37290, 1
- Evans, P. A., Beardmore, A. P., Page, K. L., et al. 2007, *A&A*, 469, 379, doi: [10.1051/0004-6361:20077530](https://doi.org/10.1051/0004-6361:20077530)
- Evans, P. A., Beardmore, A. P., Page, K. L., et al. 2009, *MNRAS*, 397, 1177, doi: [10.1111/j.1365-2966.2009.14913.x](https://doi.org/10.1111/j.1365-2966.2009.14913.x)
- Fermi GBM Team. 2024, GRB Coordinates Network, 37273, 1
- Finneran, G., Cotter, L., & Martin-Carrillo, A. 2025, *Astronomy and Computing*, 52, 100954, doi: [10.1016/j.ascom.2025.100954](https://doi.org/10.1016/j.ascom.2025.100954)
- Fishman, G. J., & Meegan, C. A. 1995, *ARA&A*, 33, 415, doi: [10.1146/annurev.aa.33.090195.002215](https://doi.org/10.1146/annurev.aa.33.090195.002215)
- Fong, W., Berger, E., & Fox, D. B. 2010, *ApJ*, 708, 9, doi: [10.1088/0004-637X/708/1/9](https://doi.org/10.1088/0004-637X/708/1/9)
- Fong, W., Berger, E., Chornock, R., et al. 2013, *ApJ*, 769, 56, doi: [10.1088/0004-637X/769/1/56](https://doi.org/10.1088/0004-637X/769/1/56)
- Fong, W.-f., Nugent, A. E., Dong, Y., et al. 2022, *ApJ*, 940, 56, doi: [10.3847/1538-4357/ac91d0](https://doi.org/10.3847/1538-4357/ac91d0)
- Fontana, A., Dunlop, J. S., Paris, D., et al. 2014, *A&A*, 570, A11, doi: [10.1051/0004-6361/201423543](https://doi.org/10.1051/0004-6361/201423543)
- Frederiks, D., Lysenko, A., Ridnaia, A., et al. 2024, GRB Coordinates Network, 37302, 1
- Fruchter, A. S., Levan, A. J., Strolger, L., et al. 2006a, *Nature*, 441, 463, doi: [10.1038/nature04787](https://doi.org/10.1038/nature04787)
- Fruchter, A. S., Levan, A. J., Strolger, L., et al. 2006b, *Nature*, 441, 463, doi: [10.1038/nature04787](https://doi.org/10.1038/nature04787)
- Fynbo, J. P. U., Watson, D., Thöne, C. C., et al. 2006, *Nature*, 444, 1047, doi: [10.1038/nature05375](https://doi.org/10.1038/nature05375)
- Galama, T. J., Vreeswijk, P. M., van Paradijs, J., et al. 1998, *Nature*, 395, 670, doi: [10.1038/27150](https://doi.org/10.1038/27150)
- Gao, H., Lei, W.-H., Zou, Y.-C., Wu, X.-F., & Zhang, B. 2013, *NewAR*, 57, 141, doi: [10.1016/j.newar.2013.10.001](https://doi.org/10.1016/j.newar.2013.10.001)
- Gehrels, N., Norris, J. P., Barthelmy, S. D., et al. 2006, *Nature*, 444, 1044, doi: [10.1038/nature05376](https://doi.org/10.1038/nature05376)
- Giallongo, E., Ragazzoni, R., Grazian, A., et al. 2008, *A&A*, 482, 349, doi: [10.1051/0004-6361:20078402](https://doi.org/10.1051/0004-6361:20078402)
- Goldstein, A., Veres, P., Burns, E., et al. 2017, *ApJL*, 848, L14, doi: [10.3847/2041-8213/aa8f41](https://doi.org/10.3847/2041-8213/aa8f41)
- Golkhou, V. Z., Butler, N. R., & Littlejohns, O. M. 2015, *ApJ*, 811, 93, doi: [10.1088/0004-637X/811/2/93](https://doi.org/10.1088/0004-637X/811/2/93)
- Gompertz, B. P., O’Brien, P. T., & Wynn, G. A. 2014, *MNRAS*, 438, 240, doi: [10.1093/mnras/stt2165](https://doi.org/10.1093/mnras/stt2165)
- Gupta, R. 2023, arXiv e-prints, arXiv:2312.16265, doi: [10.48550/arXiv.2312.16265](https://doi.org/10.48550/arXiv.2312.16265)
- Gupta, R., Ror, A. K., Pandey, S. B., et al. 2024a, arXiv e-prints, arXiv:2409.04871, doi: [10.48550/arXiv.2409.04871](https://doi.org/10.48550/arXiv.2409.04871)
- Gupta, R., Oates, S. R., Pandey, S. B., et al. 2021, *MNRAS*, 505, 4086, doi: [10.1093/mnras/stab1573](https://doi.org/10.1093/mnras/stab1573)
- Gupta, R., Pandey, S. B., Kumar, A., et al. 2022a, *Journal of Astrophysics and Astronomy*, 43, 82, doi: [10.1007/s12036-022-09865-0](https://doi.org/10.1007/s12036-022-09865-0)
- Gupta, R., Gupta, S., Chattopadhyay, T., et al. 2022b, *MNRAS*, 511, 1694, doi: [10.1093/mnras/stac015](https://doi.org/10.1093/mnras/stac015)

- Gupta, R., Brivio, R., Dichiaro, S., et al. 2024b, GRB Coordinates Network, 37274, 1
- Gupta, R., Pandey, S. B., Gupta, S., et al. 2024c, ApJ, 972, 166, doi: [10.3847/1538-4357/ad5a92](https://doi.org/10.3847/1538-4357/ad5a92)
- Gupta, S., Gupta, R., Chattopadhyay, T., et al. 2025, arXiv e-prints, arXiv:2504.05038, doi: [10.48550/arXiv.2504.05038](https://doi.org/10.48550/arXiv.2504.05038)
- Hjorth, J., Sollerman, J., Møller, P., et al. 2003, Nature, 423, 847, doi: [10.1038/nature01750](https://doi.org/10.1038/nature01750)
- Hu, Y. D., Castro-Tirado, A. J., Kumar, A., et al. 2021, A&A, 646, A50, doi: [10.1051/0004-6361/202039349](https://doi.org/10.1051/0004-6361/202039349)
- Hu, Y. D., Fernández-García, E., Caballero-García, M. D., et al. 2023, Frontiers in Astronomy and Space Sciences, 10, 952887, doi: [10.3389/fspas.2023.952887](https://doi.org/10.3389/fspas.2023.952887)
- Hunt, L. K., Palazzi, E., Michałowski, M. J., et al. 2014, A&A, 565, A112, doi: [10.1051/0004-6361/201323340](https://doi.org/10.1051/0004-6361/201323340)
- Iwamoto, K., Mazzali, P. A., Nomoto, K., et al. 1998, Nature, 395, 672, doi: [10.1038/27155](https://doi.org/10.1038/27155)
- Izzo, L., & Malesani, D. B. 2024, GRB Coordinates Network, 37287, 1
- Izzo, L., de Ugarte Postigo, A., Maeda, K., et al. 2019, Nature, 565, 324, doi: [10.1038/s41586-018-0826-3](https://doi.org/10.1038/s41586-018-0826-3)
- Japelj, J., Vergani, S. D., Salvaterra, R., et al. 2016, A&A, 590, A129, doi: [10.1051/0004-6361/201628314](https://doi.org/10.1051/0004-6361/201628314)
- Jespersen, C. K., Severin, J. B., Steinhardt, C. L., et al. 2020, ApJL, 896, L20, doi: [10.3847/2041-8213/ab964d](https://doi.org/10.3847/2041-8213/ab964d)
- Joshi, J., Waratkar, G., Vibhute, A., et al. 2024, GRB Coordinates Network, 37298, 1
- Kalberla, P. M. W., Burton, W. B., Hartmann, D., et al. 2005, Astronomy & Astrophysics, 440, 775, doi: [10.1051/0004-6361:20041864](https://doi.org/10.1051/0004-6361:20041864)
- Kann, D. A., Klose, S., & Zeh, A. 2006, ApJ, 641, 993, doi: [10.1086/500652](https://doi.org/10.1086/500652)
- Kann, D. A., Klose, S., Zhang, B., et al. 2010, ApJ, 720, 1513, doi: [10.1088/0004-637X/720/2/1513](https://doi.org/10.1088/0004-637X/720/2/1513)
- Klebesadel, R. W., Strong, I. B., & Olson, R. A. 1973, ApJL, 182, L85, doi: [10.1086/181225](https://doi.org/10.1086/181225)
- Kouveliotou, C., Meegan, C. A., Fishman, G. J., et al. 1993, ApJL, 413, L101, doi: [10.1086/186969](https://doi.org/10.1086/186969)
- Krühler, T., Greiner, J., Schady, P., et al. 2011, A&A, 534, A108, doi: [10.1051/0004-6361/201117428](https://doi.org/10.1051/0004-6361/201117428)
- Kuin, N. P. M., Gupta, R., & Swift/UVOT Team. 2024, GRB Coordinates Network, 37296, 1
- Kumar, P., & Panaitescu, A. 2000, ApJL, 541, L51, doi: [10.1086/312905](https://doi.org/10.1086/312905)
- Kumar, P., & Zhang, B. 2015, PhR, 561, 1, doi: [10.1016/j.physrep.2014.09.008](https://doi.org/10.1016/j.physrep.2014.09.008)
- Le Floc'h, E., Adami, C., Schneider, B., et al. 2024, GRB Coordinates Network, 37300, 1
- Levan, A. J., Gompertz, B. P., Salafia, O. S., et al. 2024, Nature, 626, 737, doi: [10.1038/s41586-023-06759-1](https://doi.org/10.1038/s41586-023-06759-1)
- Li, Q. M., Sun, Q. B., Zhang, Z. B., Zhang, K. J., & Long, G. 2024, MNRAS, 527, 7111, doi: [10.1093/mnras/stad3619](https://doi.org/10.1093/mnras/stad3619)
- Li, Y., Shen, R.-F., & Zhang, B.-B. 2023, ApJ, 955, 98, doi: [10.3847/1538-4357/acefbf](https://doi.org/10.3847/1538-4357/acefbf)
- Lien, A., Sakamoto, T., Barthelmy, S. D., et al. 2016, ApJ, 829, 7, doi: [10.3847/0004-637X/829/1/7](https://doi.org/10.3847/0004-637X/829/1/7)
- Lü, H.-J., Liang, E.-W., Zhang, B.-B., & Zhang, B. 2010, ApJ, 725, 1965, doi: [10.1088/0004-637X/725/2/1965](https://doi.org/10.1088/0004-637X/725/2/1965)
- Lü, H.-J., Yuan, H.-Y., Yi, T.-F., et al. 2022, ApJL, 931, L23, doi: [10.3847/2041-8213/ac6e3a](https://doi.org/10.3847/2041-8213/ac6e3a)
- Luo, J.-W., Wang, F.-F., Zhu-Ge, J.-M., et al. 2023, ApJ, 959, 44, doi: [10.3847/1538-4357/ad03ec](https://doi.org/10.3847/1538-4357/ad03ec)
- MacFadyen, A. I., & Woosley, S. E. 1999, ApJ, 524, 262, doi: [10.1086/307790](https://doi.org/10.1086/307790)
- MacLachlan, G. A., Shenoy, A., Sonbas, E., et al. 2013, MNRAS, 432, 857, doi: [10.1093/mnras/stt241](https://doi.org/10.1093/mnras/stt241)
- Madau, P. 1995, ApJ, 441, 18, doi: [10.1086/175332](https://doi.org/10.1086/175332)
- Martin-Carrillo, A., Schneider, B., Pugliese, G., et al. 2024, GRB Coordinates Network, 37293, 1
- Mazzali, P. A., Deng, J., Tominaga, N., et al. 2003, ApJL, 599, L95, doi: [10.1086/381259](https://doi.org/10.1086/381259)
- Metzger, B. D., Quataert, E., & Thompson, T. A. 2008, MNRAS, 385, 1455, doi: [10.1111/j.1365-2966.2008.12923.x](https://doi.org/10.1111/j.1365-2966.2008.12923.x)
- Minaev, P. Y., & Pozanenko, A. S. 2020, MNRAS, 492, 1919, doi: [10.1093/mnras/stz3611](https://doi.org/10.1093/mnras/stz3611)
- Misra, K., Resmi, L., Kann, D. A., et al. 2021, MNRAS, 504, 5685, doi: [10.1093/mnras/stab1050](https://doi.org/10.1093/mnras/stab1050)
- Moss, M., Lien, A., Guiriec, S., Cenko, S. B., & Sakamoto, T. 2022, ApJ, 927, 157, doi: [10.3847/1538-4357/ac4d94](https://doi.org/10.3847/1538-4357/ac4d94)
- Moss, M. J., Barthelmy, S. D., Gupta, R., et al. 2024, GRB Coordinates Network, 37355, 1
- Nakar, E. 2007, PhR, 442, 166, doi: [10.1016/j.physrep.2007.02.005](https://doi.org/10.1016/j.physrep.2007.02.005)
- Negro, M., Cibrario, N., Burns, E., et al. 2025, ApJ, 981, 14, doi: [10.3847/1538-4357/ada8a9](https://doi.org/10.3847/1538-4357/ada8a9)
- Neubert, T., Østgaard, N., Reglero, V., et al. 2019, arXiv e-prints, arXiv:1906.12178, doi: [10.48550/arXiv.1906.12178](https://doi.org/10.48550/arXiv.1906.12178)
- Norris, J. P. 2002, ApJ, 579, 386, doi: [10.1086/342747](https://doi.org/10.1086/342747)
- Norris, J. P., & Bonnell, J. T. 2006, ApJ, 643, 266, doi: [10.1086/502796](https://doi.org/10.1086/502796)
- Norris, J. P., Marani, G. F., & Bonnell, J. T. 2000, ApJ, 534, 248, doi: [10.1086/308725](https://doi.org/10.1086/308725)
- Nuessle, P., Racusin, J. L., & White, N. E. 2024, ApJ, 974, 120, doi: [10.3847/1538-4357/ad6a56](https://doi.org/10.3847/1538-4357/ad6a56)

- Nugent, A. E., Fong, W.-F., Dong, Y., et al. 2022, *ApJ*, 940, 57, doi: [10.3847/1538-4357/ac91d1](https://doi.org/10.3847/1538-4357/ac91d1)
- Panaiteescu, A., & Kumar, P. 2004, *MNRAS*, 353, 511, doi: [10.1111/j.1365-2966.2004.08083.x](https://doi.org/10.1111/j.1365-2966.2004.08083.x)
- Piran, T. 2004, *Reviews of Modern Physics*, 76, 1143, doi: [10.1103/RevModPhys.76.1143](https://doi.org/10.1103/RevModPhys.76.1143)
- Poolakkil, S., Preece, R., Fletcher, C., et al. 2021, *ApJ*, 913, 60, doi: [10.3847/1538-4357/abf24d](https://doi.org/10.3847/1538-4357/abf24d)
- Poole, T. S., Breeveld, A. A., Page, M. J., et al. 2008, *Monthly Notices of the Royal Astronomical Society*, 383, 627, doi: [10.1111/j.1365-2966.2007.12563.x](https://doi.org/10.1111/j.1365-2966.2007.12563.x)
- Preece, R. D., Briggs, M. S., Mallozzi, R. S., et al. 2000, *ApJS*, 126, 19, doi: [10.1086/313289](https://doi.org/10.1086/313289)
- Prentice, S. J., Mazzali, P. A., Pian, E., et al. 2016, *MNRAS*, 458, 2973, doi: [10.1093/mnras/stw299](https://doi.org/10.1093/mnras/stw299)
- Qin, Y., Liang, E.-W., Liang, Y.-F., et al. 2013, *ApJ*, 763, 15, doi: [10.1088/0004-637X/763/1/15](https://doi.org/10.1088/0004-637X/763/1/15)
- Qin, Y.-P., & Chen, Z.-F. 2013, *MNRAS*, 430, 163, doi: [10.1093/mnras/sts547](https://doi.org/10.1093/mnras/sts547)
- Rastinejad, J. C., Gompertz, B. P., Levan, A. J., et al. 2022, *Nature*, 612, 223, doi: [10.1038/s41586-022-05390-w](https://doi.org/10.1038/s41586-022-05390-w)
- Romanov, F. D. 2024, *GRB Coordinates Network*, 37335, 1
- Roming, P. W. A., Kennedy, T. E., Mason, K. O., et al. 2005, *SSRv*, 120, 95, doi: [10.1007/s11214-005-5095-4](https://doi.org/10.1007/s11214-005-5095-4)
- Rossi, A., Rothberg, B., Palazzi, E., et al. 2022, *ApJ*, 932, 1, doi: [10.3847/1538-4357/ac60a2](https://doi.org/10.3847/1538-4357/ac60a2)
- Ruffini, R., Bianco, C. L., Della Valle, M., et al. 2024, *GRB Coordinates Network*, 37536, 1
- Sánchez-Ramírez, R., Lang, R. G., Pozanenko, A., et al. 2024, *A&A*, 692, A3, doi: [10.1051/0004-6361/202449783](https://doi.org/10.1051/0004-6361/202449783)
- Sari, R., & Piran, T. 1999, *ApJ*, 520, 641, doi: [10.1086/307508](https://doi.org/10.1086/307508)
- Sari, R., Piran, T., & Narayan, R. 1998, *ApJL*, 497, L17, doi: [10.1086/311269](https://doi.org/10.1086/311269)
- Savaglio, S., Glazebrook, K., & Le Borgne, D. 2006, in *American Institute of Physics Conference Series*, Vol. 836, *Gamma-Ray Bursts in the Swift Era*, ed. S. S. Holt, N. Gehrels, & J. A. Nousek (AIP), 540–545, doi: [10.1063/1.2207951](https://doi.org/10.1063/1.2207951)
- Savaglio, S., Glazebrook, K., & Le Borgne, D. 2009, *ApJ*, 691, 182, doi: [10.1088/0004-637X/691/1/182](https://doi.org/10.1088/0004-637X/691/1/182)
- Schady, P., Mason, K. O., Page, M. J., et al. 2007, *Monthly Notices of the Royal Astronomical Society*, 377, 273, doi: [10.1111/j.1365-2966.2007.11592.x](https://doi.org/10.1111/j.1365-2966.2007.11592.x)
- Schady, P., Page, M. J., Oates, S. R., et al. 2010, *MNRAS*, 401, 2773, doi: [10.1111/j.1365-2966.2009.15861.x](https://doi.org/10.1111/j.1365-2966.2009.15861.x)
- Schady, P., Dwelly, T., Page, M. J., et al. 2012, *A&A*, 537, A15, doi: [10.1051/0004-6361/201117414](https://doi.org/10.1051/0004-6361/201117414)
- Schlaafly, E. F., & Finkbeiner, D. P. 2011, *ApJ*, 737, 103, doi: [10.1088/0004-637X/737/2/103](https://doi.org/10.1088/0004-637X/737/2/103)
- Schlegel, D. J., Finkbeiner, D. P., & Davis, M. 1998, *The Astrophysical Journal*, 500, 525, doi: [10.1086/305772](https://doi.org/10.1086/305772)
- Soderberg, A. M., Chakraborti, S., Pignata, G., et al. 2010, *Nature*, 463, 513, doi: [10.1038/nature08714](https://doi.org/10.1038/nature08714)
- Starling, R. L. C., Wiersema, K., Levan, A. J., et al. 2011, *MNRAS*, 411, 2792, doi: [10.1111/j.1365-2966.2010.17879.x](https://doi.org/10.1111/j.1365-2966.2010.17879.x)
- Stratta, G., Nicuesa Guelbenzu, A. M., Klose, S., et al. 2025, *ApJ*, 979, 159, doi: [10.3847/1538-4357/ad9b7b](https://doi.org/10.3847/1538-4357/ad9b7b)
- Sun, H., Wang, C. W., Yang, J., et al. 2025, *National Science Review*, 12, nwae401, doi: [10.1093/nsr/nwae401](https://doi.org/10.1093/nsr/nwae401)
- SVOM/C-GFT Team, Chao Wu, Kang, Z., et al. 2024, *GRB Coordinates Network*, 37373, 1
- Taggart, K., & Perley, D. A. 2021, *MNRAS*, 503, 3931, doi: [10.1093/mnras/stab174](https://doi.org/10.1093/mnras/stab174)
- Troja, E., Fryer, C. L., O'Connor, B., et al. 2022, *Nature*, 612, 228, doi: [10.1038/s41586-022-05327-3](https://doi.org/10.1038/s41586-022-05327-3)
- Ukwatta, T. N., Stamatikos, M., Dhuga, K. S., et al. 2010, *ApJ*, 711, 1073, doi: [10.1088/0004-637X/711/2/1073](https://doi.org/10.1088/0004-637X/711/2/1073)
- Valenti, S., Benetti, S., Cappellaro, E., et al. 2008, *MNRAS*, 383, 1485, doi: [10.1111/j.1365-2966.2007.12647.x](https://doi.org/10.1111/j.1365-2966.2007.12647.x)
- van Dokkum, P. G. 2001, *PASP*, 113, 1420, doi: [10.1086/323894](https://doi.org/10.1086/323894)
- Veres, P., Bhat, P. N., Burns, E., et al. 2023, *ApJL*, 954, L5, doi: [10.3847/2041-8213/ace82d](https://doi.org/10.3847/2041-8213/ace82d)
- Villar, V. A., Guillochon, J., Berger, E., et al. 2017, *ApJL*, 851, L21, doi: [10.3847/2041-8213/aa9c84](https://doi.org/10.3847/2041-8213/aa9c84)
- Volnova, A., Pozanenko, A., Mazaeva, E., et al. 2021, *Anais da Academia Brasileira de Ciencias*, 93, doi: [/10.1590/0001-3765202102000883](https://doi.org/10.1590/0001-3765202102000883)
- von Kienlin, A., Meegan, C. A., Paciesas, W. S., et al. 2020, *ApJ*, 893, 46, doi: [10.3847/1538-4357/ab7a18](https://doi.org/10.3847/1538-4357/ab7a18)
- Wang, B. T., Song, F. F., Li, R. Z., et al. 2024, *GRB Coordinates Network*, 37306, 1
- Wang, C.-W., Xiong, S.-L., & Gecam Team. 2024, *GRB Coordinates Network*, 37315, 1
- Wang, X. I., Zhang, B.-B., & Lei, W.-H. 2022, *ApJL*, 931, L2, doi: [10.3847/2041-8213/ac6c7e](https://doi.org/10.3847/2041-8213/ac6c7e)
- Woosley, S. E. 1993, *ApJ*, 405, 273, doi: [10.1086/172359](https://doi.org/10.1086/172359)
- Woosley, S. E., & Bloom, J. S. 2006, *ARA&A*, 44, 507, doi: [10.1146/annurev.astro.43.072103.150558](https://doi.org/10.1146/annurev.astro.43.072103.150558)
- Wu, C., Wang, Y., Li, H.-L., et al. 2025, *arXiv e-prints*, arXiv:2507.02806, doi: [10.48550/arXiv.2507.02806](https://doi.org/10.48550/arXiv.2507.02806)
- Xiao, S., Zhang, Y.-Q., Zhu, Z.-P., et al. 2024, *ApJ*, 970, 6, doi: [10.3847/1538-4357/ad4ee1](https://doi.org/10.3847/1538-4357/ad4ee1)
- Yang, J., Ai, S., Zhang, B.-B., et al. 2022, *Nature*, 612, 232, doi: [10.1038/s41586-022-05403-8](https://doi.org/10.1038/s41586-022-05403-8)
- Zhang, B. 2025, *Journal of High Energy Astrophysics*, 45, 325, doi: [10.1016/j.jheap.2024.12.013](https://doi.org/10.1016/j.jheap.2024.12.013)

Zhang, B., Fan, Y. Z., Dyks, J., et al. 2006, *ApJ*, 642, 354,
doi: [10.1086/500723](https://doi.org/10.1086/500723)

Zhang, B., & Kobayashi, S. 2005, *ApJ*, 628, 315,
doi: [10.1086/429787](https://doi.org/10.1086/429787)

Zhang, B., & Mészáros, P. 2004, *International Journal of
Modern Physics A*, 19, 2385,
doi: [10.1142/S0217751X0401746X](https://doi.org/10.1142/S0217751X0401746X)

Zhang, B., Zhang, B.-B., Virgili, F. J., et al. 2009, *ApJ*,
703, 1696, doi: [10.1088/0004-637X/703/2/1696](https://doi.org/10.1088/0004-637X/703/2/1696)

Zhang, Z.-B., Yang, E.-B., Choi, C.-S., & Chang, H.-Y.
2016, *MNRAS*, 462, 3243, doi: [10.1093/mnras/stw1835](https://doi.org/10.1093/mnras/stw1835)

Zhu, S.-Y., Sun, W.-P., Ma, D.-L., & Zhang, F.-W. 2024,
MNRAS, 532, 1434, doi: [10.1093/mnras/stae1594](https://doi.org/10.1093/mnras/stae1594)